

Version 2 data of the National Science Foundation's Ultraviolet Radiation Monitoring Network: South Pole

G. Bernhard, C. R. Booth, and J. C. Eshamjian

Biospherical Instruments Inc., San Diego, California, USA

Received 20 April 2004; revised 15 July 2004; accepted 3 August 2004; published 12 November 2004.

[1] Spectral ultraviolet (UV) and visible irradiance has been measured at the South Pole between 1991 and 2003 by a SUV-100 spectroradiometer, which is part of the U.S. National Science Foundation's UV Monitoring Network. Here we present a new data edition, labeled "Version 2." The new version was corrected for wavelength shift errors and deviations of the spectroradiometer from the ideal cosine response. A comprehensive uncertainty budget of the new data set was established. Below 400 nm the expanded standard uncertainty (coverage factor 2) varies between 4.6 and 7.2%, depending on wavelength and sky condition. The uncertainty of biologically relevant UV irradiances is approximately 6%. Compared to the previously published data set, Version 2 UV data are higher by 5–14%, depending on wavelength, solar zenith angle (SZA), and year of observation. By comparing Version 2 data with results of a radiative transfer model, the good consistency and homogeneity of the new data set were confirmed. The data set is used to establish a UV climatology for the South Pole, focusing on the effects of aerosols, clouds, and total column ozone. Clouds are predominantly optically thin; 71% of all clouds have an optical depth between 0 and 1. The average attenuation of UV irradiance at 345 nm by clouds is less than 5% and no attenuations greater than 23% were observed. Attenuation by homogeneous clouds is generally larger in the visible than in the UV. The wavelength dependence of cloud attenuation is quantitatively explained with the wavelength-dependent radiance distribution on top of clouds and the incidence-angle dependence of cloud transmittance. Largest radiation levels occur in late November and early December when low stratospheric ozone amounts coincide with relatively small SZAs. Owing to the large effect of the "ozone hole," short- and long-term variability of UV during the austral spring is very high. When the ozone hole disappears, DNA-damaging irradiance can decrease by more than a factor of two within 2 days. Typical summer UV index values range between 2 and 3.5 and vary by $\pm 30\%$ ($\pm 1\sigma$) between different years. Linear regression analyses did not indicate statistically significant UV trends owing to the large year-to-year variability and the fact that the network was established only after the first occurrence of the ozone hole. Current measurements therefore document variability on an elevated level. *INDEX TERMS*: 0360 Atmospheric Composition and Structure: Transmission and scattering of radiation; 0394 Atmospheric Composition and Structure: Instruments and techniques; 3359 Meteorology and Atmospheric Dynamics: Radiative processes; *KEYWORDS*: ultraviolet radiation, UV, Antarctica, South Pole, uncertainty, total column ozone

Citation: Bernhard, G., C. R. Booth, and J. C. Eshamjian (2004), Version 2 data of the National Science Foundation's Ultraviolet Radiation Monitoring Network: South Pole, *J. Geophys. Res.*, 109, D21207, doi:10.1029/2004JD004937.

1. Introduction

[2] Most technical parts of this paper are provided in an electronic supplement¹. For ease of reading, the section numbering in the supplement follows that in the main paper. References to supplementary material (sections, equations, figures, etc.) are all prefixed with a capital S.

[3] The National Science Foundation Office of Polar Programs (NSF/OPP) Ultraviolet Radiation Monitoring

Network was established in 1987 in response to severe ozone depletion reported in Antarctica. Biospherical Instruments (BSI) installed the first instruments in 1988 and has operated the network since then. The network currently consists of three sites in Antarctica (Amundsen-Scott South Pole Station (90°S), McMurdo Station (77° 50'S, 166° 40'E), Palmer Station (64° 46'S, 64° 03'W)); one site in Ushuaia, Argentina (54° 49'S, 68° 19'W); and

two boreal locations (San Diego, CA ($32^{\circ} 46'N$, $117^{\circ} 12'W$), Barrow, AK ($71^{\circ} 19'N$, $156^{\circ} 41'W$)). All stations are equipped with high-resolution SUV-100 spectroradiometers. Measurements of global spectral irradiance between 280 and 600 nm are performed quarter hourly when the solar zenith angle (SZA) is smaller than 93° . An overview of the network including locations, instrumentation, measurement protocols, data analysis methods, quality control procedures, and example data can be found in the work of *Booth et al.* [1994], Network Operations Reports [e.g., *Bernhard et al.*, 2003a], and at the Website www.biospherical.com/nsf. Data are organized in volumes, which roughly span one year (see Table S3 and Figure S7 for period assignment), and are distributed via CD-ROM and the Website www.biospherical.com/nsf.

[4] Network data have been used by dozens of researchers. A comprehensive list of applications is provided in section S1 of the supplement. All published results were based on the originally released “Version 0” network data set. This data set has not been corrected for deviations of the angular response of SUV-100 spectroradiometers from the ideal cosine response and therefore underestimates the actual irradiance. Version 0 data are also not corrected for an azimuth angle dependence of the instruments’ angular response, which affected data measured before the year 2000 when the instruments’ entrance optics were upgraded. Spectra measured before 1997 exhibit a wavelength error of approximately 0.1 nm [*Bernhard et al.*, 2003a], which lead to underestimation of UV-B radiation. Changes to hardware and software introduced over the years of operation lead to additional step changes in data time series.

[5] To improve the accuracy of network data, a new data version, named “Version 2” has been generated. This paper introduces the new version for measurements from the instrument located at the South Pole (SPO).

[6] Version 2 spectra have been corrected for wavelength errors and the cosine error, which describes the deviation of the spectroradiometer’s angular dependence from the ideal cosine response. Moreover, Version 2 spectra have been normalized to a standard resolution of 1.0 nm full width at half maximum (FWHM) with triangular band pass, and are now provided on a uniform wavelength grid. The corrections improved the homogeneity of the data set by removing systematic errors and discontinuities in data time series. Version 2 data feature also a larger number of data products such as total column ozone, and cloud optical depth. A complete listing of data products is provided in section S8 of the supplement.¹

[7] Model calculations are an integral part of Version 2. They provide clear-sky reference spectra during cloudy periods and are a prerequisite for the different corrections. Version 2 data are therefore no longer “pure” measurements like Version 0 data. Rather, measurements were combined with model calculations to produce the best estimate of solar irradiance at the time and place of the measurement.

[8] Currently Version 2 data are available only for SPO as data processing requires several months for each site. We are planning to provide Version 2 data for other network sites in the future. We decided to process SPO data first,

since the South Pole is a very interesting place for UV measurements due to the annually recurring “ozone hole,” stable meteorological conditions, frequent cloudless days, constant high surface albedo, little aerosol influence, negligible air pollution, and virtually no diurnal change of SZA. In addition, important input parameters for the corrections, such as total column ozone and the atmospheric ozone profile, are available from measurements of NOAA’s Climate Monitoring and Diagnostics Laboratory (CMDL) facility at SPO.

[9] The paper is organized as follows: Section 2 describes corrections that have been applied in the generation of Version 2. Section 3 analyzes the uncertainties of the new data set, and section 4 compares Version 2 with Version 0. In section 5, Version 2 spectra are compared with results of the radiative transfer model with special emphasis given to the influence of aerosols and the impact of the extraterrestrial spectrum used by the model. In section 6, a UV climatology for SPO is established based on the new data set, focusing on effects of total ozone and clouds on UV, and variability and long-term changes in UV. Discussion and conclusions are presented in section 7.

2. Corrections

2.1. Radiative Transfer Model

[10] Model calculations are an important part of Version 2 as they are used in the correction algorithms and for the interpretation of measurements. Every Version 2 spectrum is complemented by a model spectrum. Calculations were performed with the radiative transfer model UVSPEC/libRadtran Version 1.0-beta, available at www.libradtran.org [*Mayer et al.*, 1997]. The model’s pseudospherical disort radiative transfer solver with six streams was used.

2.1.1. Model Input Parameters

[11] Total column ozone was calculated from measured spectra using the inversion algorithm described by *Bernhard et al.* [2003b] and the *Bass and Paur* [1985] ozone absorption cross section. The ozone value returned by the algorithm was used for modeling. On average, these ozone values are high by 1.7% compared to Version 8 overpass ozone data from NASA’s Total Ozone Mapping Spectrometers (TOMS) installed on Nimbus 7 and Earth Probe satellites. There is no significant SZA-dependence between the two data sets for SZAs up to 86° . The difference between the two data sets, and also the difference from CMDL Dobson ozone data measured at SPO will be discussed elsewhere. We decided to use our ozone data for modeling as they are available for every day with spectral measurements.

[12] Air density and pressure profiles were taken from *Anderson et al.* [1986]. Ozone and temperature profiles, as well as ground pressure were taken from ozone sonde observations performed at the South Pole by NOAA/CMDL. Balloons were launched approximately every third day. Only profiles with a burst altitude of at least 30 km were used, and profiles were extrapolated to higher altitudes using an algorithm described by *Bernhard et al.* [2002]. Albedo was set to a wavelength-independent value of 0.98 as measured at SPO by *Grenfell et al.* [1994]. No aerosol extinction was considered. This simplification is acceptable as background aerosol optical depth at the South Pole are

only 0.012 [Shaw, 1982]. Modeled spectra were convolved with a triangular function with 1.0 nm FWHM.

2.1.2. Extraterrestrial Spectrum

[13] The extraterrestrial spectrum used for modeling is a composite of the spectra measured by the Solar Ultraviolet Spectral Irradiance Monitor (SUSIM) onboard the space shuttle during the ATLAS-2 and -3 missions [Kaye and Miller, 1996; vanHoosier, 1996], and the very high resolution (approximately 0.0001 nm) “Kitt Peak solar flux atlas” [Kurucz et al., 1984], measured with a Fourier transform spectroradiometer. The composite spectrum is denoted $E_*(\lambda)$ and its construction is described in detail in section S2.1.2. of the supplement.¹

2.1.3. Selection of Clear-Sky Days

[14] The data set was divided into clear-sky and non-clear-sky spectra. Spectra were regarded clear sky if variations of spectral irradiance at 600 nm from one spectrum to the next and second-next neighboring spectra were smaller than 1%. With one scan every 15 min, this means that radiation levels have to be stable within ± 30 min for a spectrum to pass the criterion. As the criterion is not based on the absolute irradiance level, it is not affected by possible calibration errors in Version 0 spectra, or the instrument’s cosine error. Spectra measured under static cloud conditions that passed the criterion could be easily identified as outliers, and were also removed from the clear-sky data set.

2.2. Wavelength Shift Correction

[15] Wavelength shifts in Version 2 spectra have been corrected by correlating the Fraunhofer line structure in measured spectra to the corresponding structure in modeled spectra. Residual wavelength uncertainties after correction are on average ± 0.04 nm ($\pm 1\sigma$) at 300 nm, ± 0.022 nm between 305 and 400 nm, ± 0.025 nm between 400 and 500 nm, and ± 0.031 nm between 500 and 590 nm. Full details of the algorithm and its accuracy can be found in section S2.2 of the supplement.¹

2.3. Cosine Error Correction

[16] The Version 2 cosine error correction is challenging since characterizations of the cosine error of the SUV-100 performed prior to deployment proved to be not applicable to the assembled and installed instrument. Solar data further suggest that the error has changed when the instrument was serviced. Moreover, the cosine error of the instrument was depending on azimuth angle and wavelength prior to a modification of the instrument’s irradiance collector in 2000. We reconstructed the cosine and azimuth errors and their change over time from measurements of a specially designed test apparatus and from comparisons of measurement and model under clear sky conditions using the Sun as light source. This method leads to larger uncertainties than the standard approach of measuring the angular response in a laboratory, but is the only feasible approach. Full details of the cosine error characterization as well as the correction algorithm and its validation can be found in section S2.3 of the supplement.¹

2.4. Bandwidth Normalization

[17] The bandwidth of SUV-100 spectroradiometers varies between 1.0 ± 0.1 nm in the UV-B and $0.8 \pm$

0.1 nm in the visible. As the SUV-100 monochromator has been exchanged several times during annual instrument service, the wavelength dependence of the bandwidth was not constant over the period of operation. This variability is problematic when spectra measured in different years or at different sites are compared. Processing Version 2 involved the normalization of all spectra to a uniform bandwidth of 1.0 nm. See section S2.4 of the supplement¹ for details.

2.5. Wavelength Resampling

[18] After wavelength correction, spectra are given on an uneven wavelength grid, which may change from one spectrum to the next. This is particularly inconvenient when comparing spectra. Processing of Version 2 therefore involved resampling to an even wavelength grid. Details of the algorithm can be found in section S2.4 of the supplement.¹

3. Uncertainty Budget

[19] The total uncertainty of Version 2 data is composed of uncertainties related to radiometric calibration and stability; cosine and azimuth error correction; the finite resolution of the spectroradiometer; residual wavelength errors after wavelength correction; nonlinearity; stray light; and photon and electronic noise. The contributions of these components have been analyzed in detail and the results are summarized in section S3 of the supplement. The combined uncertainty of Version 2 SPO data was calculated and is presented in Table 1. Expanded relative uncertainties (coverage factor $k = 2$) vary between 4.6% and 13.4%. Expanded uncertainties for spectral irradiance at 310 nm range between 6.2% and 6.4% and are dominated by uncertainties related to calibration, stability, and wavelength errors. At larger wavelengths, the greatest uncertainty arises from the insufficient knowledge of the contribution of direct irradiance to global irradiance. This is particularly a problem during periods of varying cloudiness when it is difficult to determine whether the cosine correction factor for clear or overcast sky should be applied. The uncertainty budget presented in Table 1 therefore distinguishes between the cases “clear sky,” “overcast” and “unknown sky condition.” Expanded uncertainties for spectral irradiance at 600 nm range between 4.6% for overcast conditions and 13.4% for periods with variable cloudiness. Expanded uncertainties for erythemal irradiance (i.e., spectral irradiance weighted with the action spectrum for sunburn [McKinlay and Diffey, 1987]) and DNA-damaging irradiance (action spectrum by Setlow [1974]) vary between 5.8% and 6.4%, and are only slightly influenced by sky condition.

4. Comparison of Version 0 and Version 2

[20] Version 2 data were compared with the originally released Version 0 data. A detailed comparison of the two versions is presented in section S.4 of the supplement, focusing on six spectral intervals in the UV and visible as well as erythemal [McKinlay and Diffey, 1987] and DNA-damaging [Setlow, 1974] irradiance. Differences are mostly caused by wavelength error and cosine error corrections.

Table 1. Uncertainty Budget of Version 2 Data, South Pole

Section	Error Source	Relative Standard Uncertainty, %									
		SZA = 70°					SZA = 80°				
		310 nm	400 nm	600 nm	Ery ^a	DNA ^a	310 nm	400 nm	600 nm	Ery ^a	DNA ^a
S3.1	calibration, stability	2.7	2.1	2.1	2.7	2.7	2.7	2.1	2.1	2.7	2.7
S3.4	spectral resolution	0.8	0.0	0.0	0.3	0.9	0.8	0.0	0.0	0.3	0.9
S3.5	λ - shift in UV-B	0.8	0.0	0.0	0.4	0.8	0.8	0.0	0.0	0.4	0.8
S3.5	λ - shift + Fraunhofer lines	0.4	0.3	0.1	0.0	0.0	0.4	0.3	0.1	0.0	0.0
S3.6	nonlinearity	0.5	0.5	0.5	0.5	0.5	0.5	0.5	0.5	0.5	0.5
S3.7	stray light	0.0	0.0	0.0	0.0	0.0	0.0	0.0	0.0	0.0	0.0
S3.8	noise	0.7	0.4	0.4	0.1	0.3	0.7	0.4	0.4	0.1	0.3
<i>Additional Uncertainties for Clear-Sky Conditions</i>											
S3.2	cosine error	0.7	1.2	1.8	0.7	0.7	0.7	1.5	3.6	0.7	0.7
S3.3	azimuth error	0.3	0.8	1.5	0.3	0.3	0.3	0.8	1.5	0.3	0.3
Combined uncertainty		3.2	2.6	3.2	2.9	3.1	3.2	2.8	4.6	2.9	3.1
Expanded uncertainty, k = 2		6.4	5.2	6.4	5.8	6.2	6.4	5.6	9.0	5.8	6.2
<i>Additional Uncertainties for Overcast Conditions</i>											
S3.2	cosine error	0.7	0.7	0.7	0.7	0.7	0.7	0.7	0.7	0.7	0.7
Combined uncertainty		3.1	2.3	2.3	2.9	3.1	3.1	2.3	2.3	2.9	3.1
Expanded uncertainty, k = 2		6.2	4.6	4.6	5.8	6.2	6.2	4.6	4.6	5.8	6.2
<i>Additional Uncertainties if Sky Condition is Unknown</i>											
S3.2	cosine error	1.0	1.9	2.8	1.0	1.0	1.0	2.7	6.2	1.0	1.0
S3.3	azimuth error	0.3	0.8	1.5	0.3	0.3	0.3	0.8	1.5	0.3	0.3
Combined uncertainty		3.2	3.0	3.9	3.0	3.2	3.2	3.6	6.8	3.0	3.2
Expanded uncertainty, k = 2		6.4	6.0	7.8	6.0	6.4	6.4	7.2	13.4	6.0	6.4

^aEry, erythral irradiance; DNA, DNA damaging irradiance. On the basis of individual uncertainties, a combined uncertainty is calculated and multiplied with a coverage factor of 2 in accordance with ISO guidelines. These final uncertainties are the quintessence of the uncertainty budget and are therefore printed in boldface.

[21] Below 310 nm, the wavelength error correction is the dominant factor due to the large increase of spectral irradiance in the ozone cutoff region of the solar spectrum. In this wavelength range, the contribution of radiation from the solar beam contributes less than 22% to global irradiance at SPO. The cosine error correction is therefore dominated by the correction factor for diffuse skies, which is smaller than 1.066 for all years, and independent of SZA.

[22] Above 310 nm, the effect of wavelength errors is small and the difference of the two versions is almost entirely due to the cosine error correction. Differences between Version 2 and 0 peak at SZAs between 75° and 85.5°, depending on the spectral band. Erythral and DNA-damaging dose rates from the Version 2 data set are between 2 and 11% higher than Version 0 data. The difference depends on SZA, year and sky condition, amongst other reasons. A similar difference is observed for UV-B irradiance (290–315 nm). Differences for UV-A irradiance range between 0 and 14%. Differences for the integral between 400 and 600 nm exceed 30% in some years at large SZAs (Figure S7). Ratios of Version 2 and Version 0 data show a different pattern before and after January 2000, when the instrument's collector was modified.

5. Comparison of Version 2 Data With Model Calculations

[23] Model results were part of the correction procedures used to produce Version 2 data. Version 2 data are therefore not independent of the model and cannot be used for rigorous model validation. The comparison of measurement and model presented below is nonetheless valuable to check the quality of Version 2 data, to test their consistency

between different years, and to discuss possible reasons for the differences between measurement and model.

5.1. Ratio of Measured and Modeled Spectra

[24] Figure 1 shows the ratio of measured Version 2 clear-sky spectra, $E_M(\lambda)$, to computed clear-sky spectra $E_C(\lambda)$ for the two-week period 1–15 November. Data from each year is presented in a separate plot. The plots show the median of $q_{V2}(\lambda) \equiv E_M(\lambda)/E_C(\lambda)$ (calculated on a wavelength-by-wavelength basis) along with the upper and lower quartile (50% range), the 90% percent range, minimum and maximum. Examination of the figure leads to the following conclusions:

[25] 1. The medians of the ratios range between 0.95 and 1.05 for all years and wavelengths above 310 nm, with the exception of the year 1991. Measurements from this year were reduced due to aerosols extinction from Cerro Hudson and Mount Pinatubo eruptions, as discussed in section 5.3.

[26] 2. The median ratios tend to be constant between 310 and 380 nm, increase by approximately 4% between 380 and 430 nm, stay approximately constant up to 500 nm, and decrease thereafter. The reasons of this wavelength dependence are further discussed in section 5.2.

[27] 3. The pattern is fairly uniform for all years but 1991. There is also no clear difference between data of the years 1992–1999, which were measured with the original cosine collector, and data of the years 2000–2002, when the modified collector was installed. This indicates that the different angular responses of the two periods are consistently treated by the correction, and that the corrections applied lead to a homogeneous data set.

[28] 4. There are distinct differences in the spread around the median for different years, expressed by the 50% and

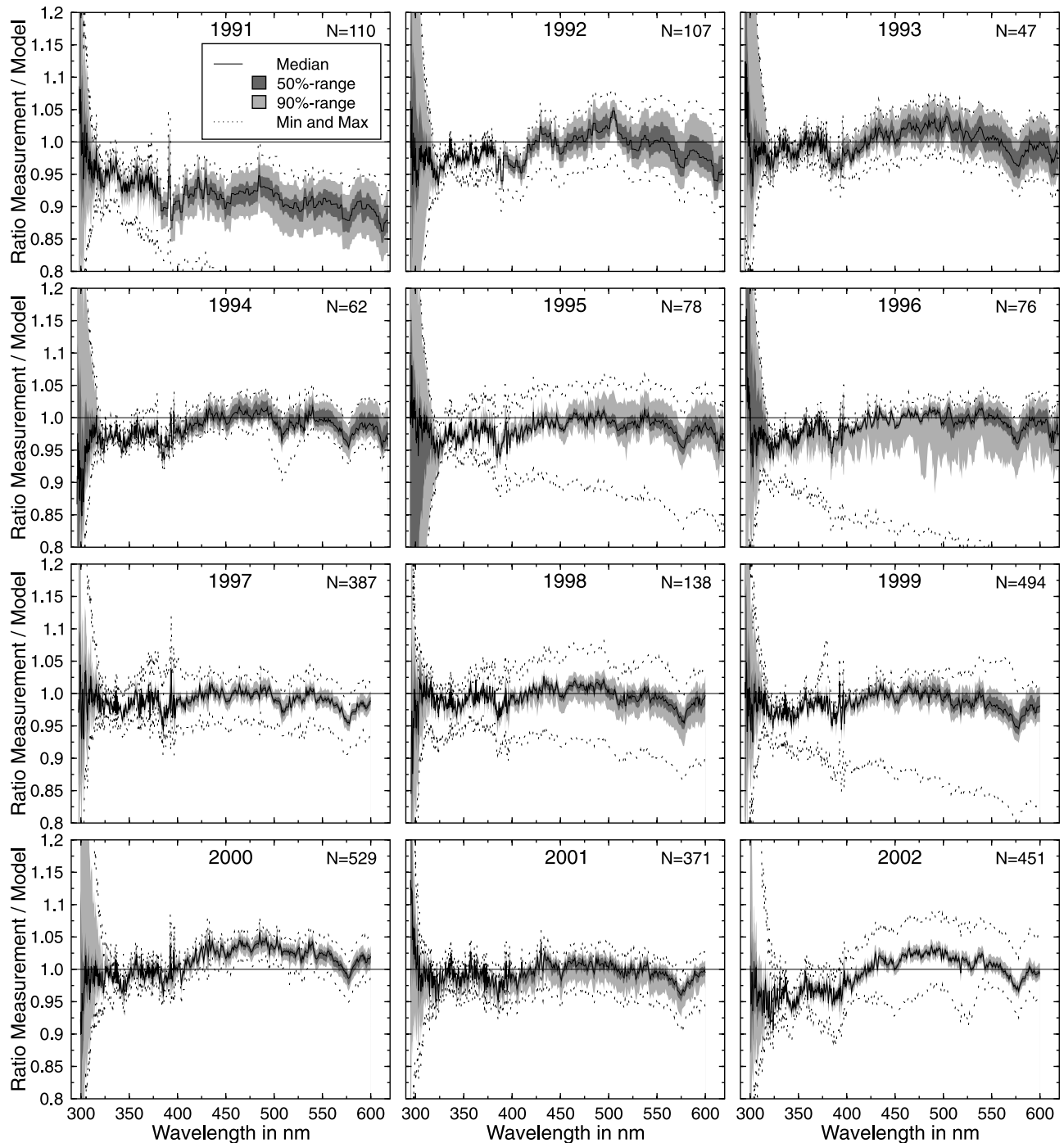


Figure 1. Ratios of clear-sky measurements to associated clear-sky model spectra for the period 1–15 November of the years 1991–2002. Each plot shows the median, 50% range, 90% range, minimum, and maximum of the ratios calculated for the year indicated in the top center of each plot. The number N of ratios used for each plot are indicated in the top right corners. N increased by a factor of four in 1997, when the duty cycle increased from one to four scans per hour.

90% ranges. The comparatively large variability in 1991–1993 is partly due to relatively large residual azimuthal errors during these years (Table S3).

[29] 5. In some years such as 1995 and 1996, the minimum and maximum ratios deviate substantially from the median. The affected spectra are likely influenced by clouds and were incorrectly included in the clear-sky subset.

This is also the likely reason for the comparatively large 90% range in 1996.

5.2. Interpretation of Measurement-Model Differences

[30] As discussed in section 5.1, the ratios of measured and modeled spectra show an increase by approximately 4% between 380 and 430 nm, stay approximately constant up to

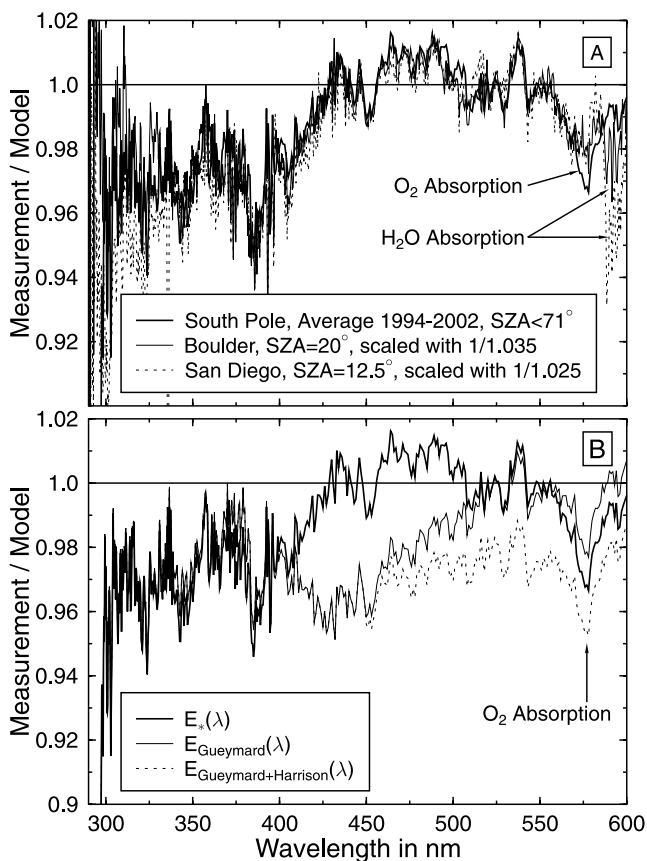


Figure 2. (a) Ratio of measurement and model for three different data sets as explained in the text. (b) Average ratio of measurement and model for Version 2 South Pole spectra. The difference in the three data sets are the extraterrestrial spectra used for the model calculations, as indicated in the legend.

500 nm, and decrease thereafter. We have seen a similar pattern at other network sites. As an example, Figure 2a compares Version 2 data from the South Pole with measurements performed with a SUV-150B spectroradiometer from BSI near Boulder, CO (40° 07'N, 105° 14'W, 1690 m a.s.l.), and San Diego. The South Pole ratio is an average ratio, defined as:

$$\bar{M}(\lambda) = \frac{1}{6} \sum_{p_i} \left(\frac{1}{9} \sum_{y=1994}^{2002} M(\lambda, p_i, y) \right), \quad (1)$$

where y is year, p_i denotes the six 2-week periods 16–31 November, and $M(\lambda, p_i, y)$ is the median of the ratio $q_{V2}(\lambda)$ between Version 2 spectra and model spectra for a given year y and period p_i , as displayed in Figure 1. Only years not affected by volcanic aerosols and only periods with SZA smaller than 71.4° were used for the construction of $\bar{M}(\lambda)$.

[31] The measurement/model ratio for Boulder was calculated for a single clear-sky spectrum, measured on 06/15/2003 during the U.S. 2003 UV Spectroradiometer Intercomparison (a publication describing the SUV-150B instruments and results of this campaign is in preparation). The SZA was 20°. Aerosol attenuation was parameterized in the model

with Ångström's turbidity formula by setting the Ångström coefficients α and β to 1.3 and 0.064, respectively, based on AERONET climatology [Holben *et al.*, 1998]. Single scattering albedo was set to $\omega = 0.96$, and surface albedo to $\gamma = 3\%$.

[32] The ratio for San Diego was measured on 5/26/03 under almost clear skies (a passing small cloud lead to a drop in the measurement between 335 and 337 nm). The SZA was 12.5°. Model parameters were set to $\alpha = 1.3$, and $\beta = 0.04$, $\omega = 0.92$, and $\gamma = 3\%$.

[33] For the comparison shown in Figure 2a, the Boulder and San Diego ratios were scaled down by 3.5% and 2.5%, respectively, to better emphasize that their spectral dependence is almost undistinguishable to $\bar{M}(\lambda)$. The bias between the three data sets is within the measurement uncertainty, but its actual cause is unknown. Preliminary analysis of the Boulder intercomparison data indicates that SUV-150B data tend to be high by 2–4%, compared to data of the two other participating groups that also have extended measurements into the visible.

[34] Despite the bias, Figure 2a demonstrates that the wavelength dependence of the three data sets is remarkably consistent considering the large differences in SZA, altitude, albedo, and atmospheric aerosol loading. Specifications of the SUV-100 and SUV-150B spectroradiometer show distinct differences: the bandwidth of the SUV-150B is 0.65 nm as opposed to 1.00 for the bandwidth-normalized Version 2 data set; the SUV-150B has a very small cosine error (for the spectra shown in Figure 2a, cosine corrections are smaller than 1% and almost independent of wavelength); and the wavelength correction of SUV-150B spectra is based on mercury lines rather than the correlation algorithm introduced in section 2.2. Lastly, the fine structure in the ratios of Figure 2a is very similar despite the fact that the South Pole data set is the average of several thousand spectra, whereas the Boulder and San Diego ratios are based on one spectrum only.

[35] Absorption by oxygen and water vapor are not considered by the model. At large SZAs, oxygen absorption lines at 580 nm and absorption by the (O₂)₂ collision complex [Naus and Ubachs, 1999] lead to a drop in the South Pole data set. Likewise, water vapor absorption is visible in the Boulder and San Diego spectra between 585 and 600 nm.

[36] The similarity of the three data sets points to a common cause, such as (1) the radiometric scale and calibration procedure, (2) systematic errors in the model to calculate atmospheric transmission, and (3) the extraterrestrial spectrum (ETS) used by the model. Uncertainties due to (1) were discussed in section S3.1 and are unlikely responsible for the spectral pattern depicted in Figure 2a.

[37] With regard to (2), it has been postulated that state-of-the-art radiative transfer models overestimate diffuse irradiance, possible due to an unknown gaseous absorber that is not accounted for in the models [Kato *et al.*, 1997]. More research indicates that there are no missing absorbers between 380 and 1000 nm [Mlawer *et al.*, 2000]. Some of the deviations could be explained by systematic errors in the measurements [Bush *et al.*, 2000], but as of 2003, some discrepancies still remain [Michalsky *et al.*, 2003]. Although the model used in our study is different from the models used by Kato *et al.* [1997] and Michalsky *et al.* [2003], there

is no final proof that it is free from errors in calculating spectral diffuse irradiance. A possible systematic model error, which is larger in the UV than in the visible, could partly explain the spectral pattern of Figure 2a. However, a mechanism that leads to the same error for the vastly different conditions presented in Figure 2a is hard to envision.

[38] We believe that the most likely reason for the observed spectral pattern is the ETS implemented in the model, $E_*(\lambda)$, as discussed in the following.

[39] After processing of Version 2 data was finished, a new ETS became available, which is a composite of 23 spectra from different sources [Gueymard, 2004]. The spectrum has the potential for becoming a reference spectrum for solar energy applications. The resolution of the spectrum is not sufficient to be used directly in the model. We therefore superimposed the fine structure from $E_*(\lambda)$ over the ETS by Gueymard [2004], to obtain the new spectrum $E_{\text{Gueymard}}(\lambda)$:

$$E_{\text{Gueymard}}(\lambda) = \frac{E_*(\lambda) \tilde{E}_G(\lambda)}{\tilde{E}_*(\lambda)}. \quad (2)$$

[40] $\tilde{E}_G(\lambda)$ and $\tilde{E}_*(\lambda)$ are the original ETS by Gueymard [2004] and the ETS defined in equation (S1), convolved with a triangular function of 20 nm FWHM, respectively.

[41] When model calculations are performed with $E_{\text{Gueymard}}(\lambda)$ the ratio of measured and modeled spectra changes by 1–4% between 400 and 520 nm (Figure 2b). Below 400 nm, the results obtained with the two ETS are very similar as both spectra are mostly based on SUSIM/ATLAS-3. The difference for wavelengths above 520 nm is less than 2%. By replacing $E_*(\lambda)$ with $E_{\text{Gueymard}}(\lambda)$, the 4% step in $q(\lambda)$ is shifted by approximately 50 nm to longer wavelengths (Figure 2b), but does not disappear.

[42] In 2003, also another ETS became available, which was extrapolated with the Langley technique [Schmid and Wehrli, 1995] from spectra measured between 360 and 1050 nm with a Rotating Shadowband Spectroradiometer [Harrison *et al.*, 2003]. Below 500 nm, the spectrum agrees to within 1.5% with $E_{\text{Gueymard}}(\lambda)$ but is higher by approximately 2% between 500 and 600 nm. If $E_{\text{Gueymard}}(\lambda)$ is used in our model below 450 nm and the spectrum by Harrison *et al.* [2003] above, the step in $q(\lambda)$ mostly disappears (broken line in Figure 2b). The good agreement (with about 3% bias) when using “ $E_{\text{Gueymard}+\text{Harrison}}(\lambda)$ ” may be fortuitous and does not rule out other courses for the spectral pattern in the ratio spectrum. However, the results indicate that the cause of the pattern can be explained by the ETS. The three ETS $E_*(\lambda)$, $E_{\text{Gueymard}}(\lambda)$, and $E_{\text{Gueymard}+\text{Harrison}}(\lambda)$ are provided in the supplement.¹

5.3. Consistency Between Different Years

[43] Clear sky spectra measured above 340 nm during periods with background aerosol conditions should show little variation from year to year due to SPO’s pristine location with constant albedo. In order to evaluate the consistency of Version 2 data between different years, we studied the ratio $q_{\text{V2}}(\lambda)$ of measured and modeled clear-sky spectra for different parts of the year. By considering $q_{\text{V2}}(\lambda)$ rather than $E_M(\lambda)$, most of the year-to-year variability

caused by total ozone amounts and by variations of SZA is removed. What remains are variations due to calibration differences, imperfect wavelength and cosine correction, and real atmospheric effects such as variation in aerosol extinction.

[44] For this analysis, we considered the ratio $Q(\lambda, p, y)$, defined as:

$$Q(\lambda, p_i, y) = \frac{M(\lambda, p_i, y)}{\frac{1}{9} \sum_{y=1994}^{2002} M(\lambda, p_i, y)}, \quad (3)$$

where $M(\lambda, p_i, y)$ is again the median of $q_{\text{V2}}(\lambda)$ for periods p_i and year y . Owing to the construction of $Q(\lambda, p_i, y)$, systematic differences between measurement and model, which affect all years equally, are ratioed out. The average in the denominator of equation (3) includes only years with background (or near-background) aerosol conditions. Results are shown in Figure 3, which consists of 12 plots for different two-week periods. $Q(\lambda, p, y)$ ratios for different years are illustrated in different grayscales.

[45] With the exceptions of the cases explained below, $Q(\lambda, p, y)$ ratios of all years and periods are within the range 1 ± 0.05 . Corrected measurements of different years are therefore consistent to within $\pm 5\%$, confirming that the corrections were successful in homogenizing the measurements of different years and in removing step changes caused by modifications to hardware and data processing methods.

[46] For the period 16–23 March, $Q(\lambda, p, y)$ ratios are only consistent to within $\pm 15\%$. During this period, SZAs are larger than 88° , therefore uncertainties in measurement, correction, model, and assessment of sky condition are substantially increased. A similar level of variation can be seen for the period after polar night, 20–30 September, when SZAs are larger than 87° (not shown in Figure 3).

[47] $Q(\lambda, p, y)$ ratios for 1991 agree well with ratios of other years for February and March, but are substantially lower in the second half of the year. The effect on global irradiance was largest immediately after polar night when UV irradiance was lower by 2–11%. Reductions in the visible exceeded 20% during October 1991 and diminish thereafter. Between December 1991, and the middle of February 1992, the attenuation was about 4–7% and independent of wavelength.

5.4. Aerosol Influence

[48] As the same cosine correction was applied to spring and fall measurements of 1991, the low $Q(\lambda, p, y)$ ratios for October–December 1991 could be caused by attenuation of solar radiation by aerosols from the Mount Pinatubo and Cerro Hudson eruptions, which occurred in June and August of 1991, respectively. The Antarctic lower stratosphere in the spring of 1991 was characterized by a layer of volcanic aerosol from the Cerro Hudson eruption [Deshler *et al.*, 1992]. After 20 September 1991, the aerosol was observed daily between 9 and 13 km by Lidar. Between October 1991 and January 1992, monthly average aerosol optical depth anomalies in the 530–690 nm range varied between 0.21 and 0.275 at SPO, according to measurements performed by CMDL

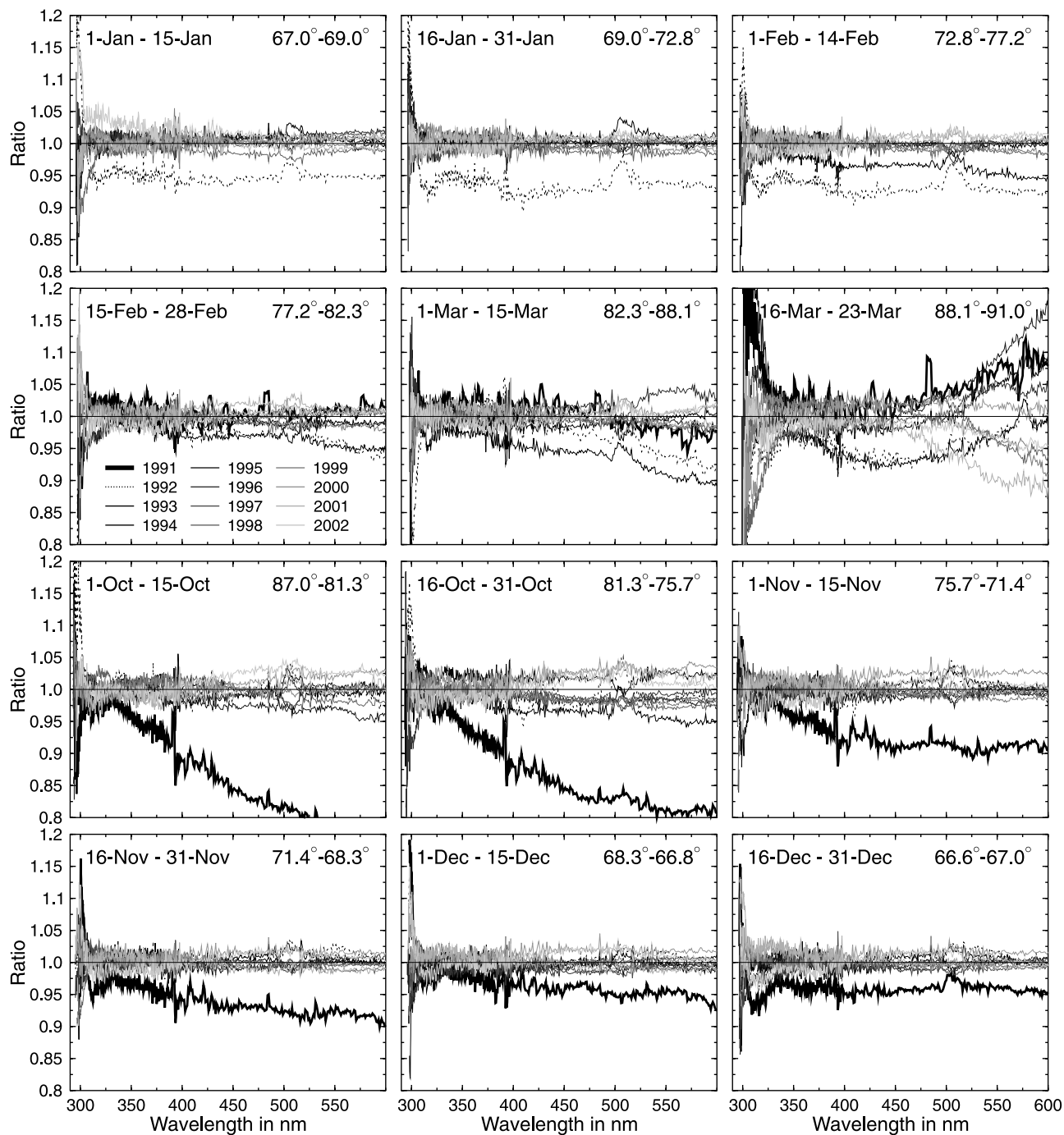


Figure 3. Normalized ratios $Q(\lambda, p, y)$ of measurement and model. Each plot shows $Q(\lambda, p, y)$ for a different two-week period, indicated in the top left corner of each plot. The SZA range for these periods is indicated in the top right corner. Data from each year are coded in a different grayscale level or color, assigned in the legend of the plot for the period 15–28 February. See color version of this figure at back of this issue.

with wideband filter wheel normal incidence pyrheliometers [Dutton and Christy, 1992; Climate Monitoring Diagnostics Laboratory (CMDL), 2002]. In order to investigate whether the effect of aerosols is large enough to explain the low $Q(\lambda, p, y)$ ratios in the spring of 1991, we modeled global irradiance with and without aerosols, and compared the results. Model calculations were performed with an aerosol layer between 9 and 13 km, an aerosol optical depth of 0.25 at

550 nm and a single scattering albedo of 0.99. The wavelength dependence of aerosol extinction was parameterized with Ångström's turbidity formula by setting the Ångström coefficient α to 0.9. The value of α was estimated with Mie calculations from the aerosol size distribution measured by Deshler *et al.* [1992] at the SPO on 8 October 1991.

[49] Figure 4 shows ratios of model spectra with and without the aerosol layer for several SZAs, which are

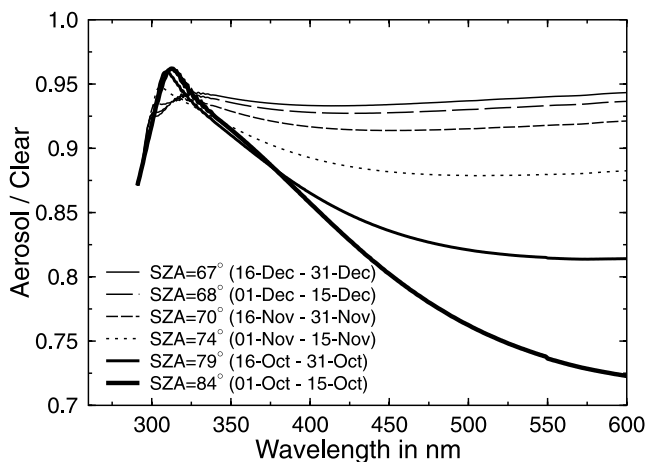


Figure 4. Ratio of model results with and without aerosols for several SZAs. Aerosols were confined to a layer between 9 and 13 km altitude and were parameterized with Ångström's turbidity formula by setting the Ångström coefficient α to 0.9 and optical depth at 550 nm to 0.25. The SZAs are representative for periods indicated in the legend. These periods are identical with those in the lower half of Figure 3.

representative of the six 2-week periods shown in the lower half of Figure 3. The effect of aerosols increases strongly with SZA. We believe that the SZA dependence has a similar reason as the SZA dependence caused by attenuation from clouds, which is discussed in section 6.1. The wave-

length-dependent aerosol attenuation shown in Figure 4 is very similar to the wavelength dependence of $Q(\lambda, p, y)$ ratios in Figure 3, suggesting, that the $Q(\lambda, p, y)$ ratio anomalies observed in the spring of 1991 could have been caused, indeed, by the Cerro Hudson aerosol.

6. UV Climatology at the South Pole

[50] After Version 2 had been generated, the data set was used to establish a climatology of UV radiation at the South Pole. Figure 5 shows time series of four Version 2 data products for the period 1991–2003. The data products are DNA-damaging radiation [Setlow, 1974], UV index, and the integrals 342.5–347.5 and 400–600 nm. The parameterization of the action spectrum for DNA is the same as implemented in the TUV radiative transfer model [Madronich, 1993]. This parameterization differs from the one used for Version 0 [Bernhard *et al.*, 2003a] and is a better fit to the original data by Setlow [1974]. UV index is an internationally recognized measure of Sun-burning UV irradiance, and is defined as spectral irradiance weighted with the CIE Erythral Action Spectrum [McKinlay and Diffey, 1987], expressed in the units of W/m^2 , and multiplied by 40 [World Meteorological Organization (WMO), 1998].

[51] DNA-damaging irradiance is very sensitive to changes in total ozone: a one percent decrease in total ozone leads to approximately a 2.2% increase in DNA-damaging irradiance [Booth and Madronich, 1994]. Most of the day-to-day variability seen in Figure 5 is due the large

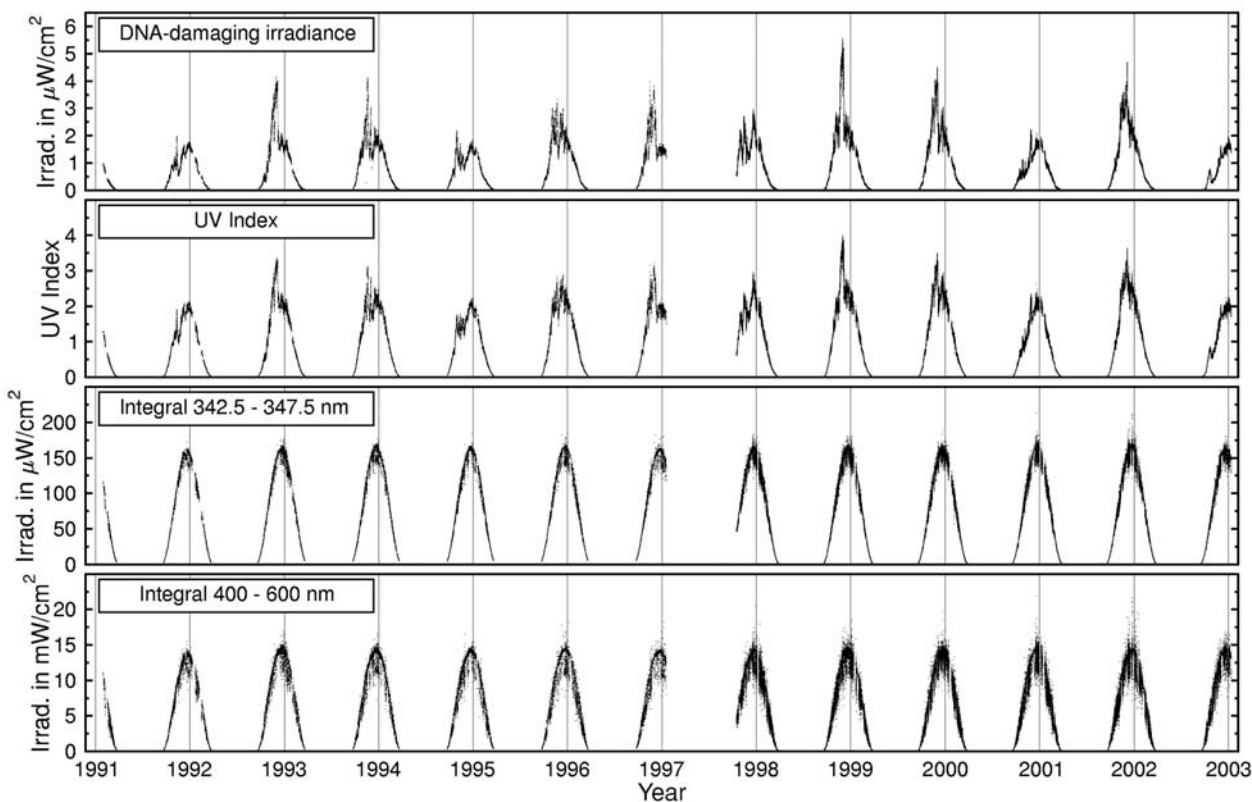


Figure 5. Time series of DNA-damaging irradiance, UV index, and integrals of 342.5–347.5 and 400–600 nm at the South Pole. Data from 1997 affected by a large offset uncertainty were not included.

variability in total ozone and the impact of the “ozone hole.” For example, radiation levels changed from $4.0 \mu\text{W}/\text{cm}^2$ on 12/5/92 to $1.8 \mu\text{W}/\text{cm}^2$ on 12/7/92 when the 1992 ozone hole closed. Largest radiation levels typically occur in late November and early December when low ozone columns coincide with relatively small SZA. Some years such as 1991, 1994, 2000, and 2003 appear to exhibit very little influence from the ozone hole, while other years such as 1992, 1993, 1996, 1998, 1999, and 2001 show a pronounced influence. This impression is somewhat deceptive as some years, such as 2000, displayed large relative enhancements in October when solar elevation and absolute values were still small. The highest DNA-damaging irradiance was measured on 11/30/98 and was $5.6 \mu\text{W}/\text{cm}^2$.

[52] The general pattern for the UV index time series of Figure 5 is similar to that of DNA-damaging irradiance. However, the variability is considerably smaller as the UV index is roughly half as sensitive to total ozone than DNA-damaging irradiance [United Nations Environment Programme (UNEP), 1991]. Typical summer UV index values range between 2 and 3.5, with a maximum value of 4.0 measured on 11/30/98. Note that these values are significantly smaller than typical summer values for midlatitudes. However, South Pole has 24 hours of daylight. Daily erythemal doses for the South Pole and San Diego, which were calculated by integrating erythemal irradiance over 24 hours, are comparable [Bernhard *et al.*, 2003a].

[53] The 342.5–347.5 nm integral is not affected by ozone and the influence by clouds is relatively small, partly because the contribution of the direct beam to global irradiance is less than 34% at all times, and partly because cloud attenuation is moderated by high albedo [Nichol *et al.*, 2003]. As a consequence, the day-to-day and year-to-year variability is very small. The plot suggests that there is less variability for the years 1991–1997 than for years 1998–2003. Until January 1997, spectra were measured hourly, from February 1997 (start of Volume 7) onward, one spectrum was measured every 15 min. The perception of larger scatter is not due to a real increase in variability but is apparent due to the four-times-higher sampling in the later years.

[54] The 400–600 nm integral is more affected by cloud attenuation than the 342.5–347.5 nm integral, which explains the higher variability. Although ozone also absorbs weakly in the visible (Chappuis band), the contribution from changes in absorption in the Chappuis band to the overall variability is negligible.

[55] The modification of the UV climate by clouds and total ozone is analyzed in more detail below.

6.1. Effect of Clouds on UV

[56] The modification of UV radiation by clouds was determined with transmittance $T(t)$, defined as

$$T(t) = \frac{E_{M,345}(t)}{E_{C,345}(t)} \bigg/ \sum_{\tilde{t} \in \{y(t), p_i(t), CS\}} \frac{1}{n} \frac{E_{M,345}(\tilde{t})}{E_{C,345}(\tilde{t})}. \quad (4)$$

$E_{M,345}(t)$ is the measured Version 2 342.5–347.5 nm integral at time t , and $E_{C,345}(t)$ is the associated clear-sky model value. The denominator of equation (4) is the average ratio of measurement and model for clear sky conditions

(“ $t \in CS$ ”) during year y and period p_i . This term removes the observed bias between measurement and model for clear skies. The correction varies between 0.9 and 1.0, depending on year and period.

[57] In the next step, $T(t)$ values for the period 1–15 January were selected from data of the years 1994–2003, and binned into 0.01-wide intervals to set up a frequency distribution for this period. Similar distributions were constructed for each period p_i , and are shown in Figure 6. Hence each plot of this figure represents the climatology of cloud transmittance relative to clear sky for a different part of the year. Measurements from the years 1991–1993 were not included due to the presence of volcanic aerosols.

[58] Distributions of all periods display a distinct maximum at $T(t) = 1$, confirming the high number of clear-sky days at the South Pole. Distributions of all periods are generally similar, but there are subtle differences. For example, the maximum is less distinct for periods with $\text{SZA} > 87^\circ$. Periods with $\text{SZA} < 80^\circ$ show a small secondary maximum at $T(t) = 0.88$. The second maximum likely includes situation where the direct beam is blocked by clouds. Average transmittance values for each period are given in the legend of each plot, and vary between 0.957 and 0.988. The average attenuation by clouds is therefore less than 5%. Transmittances of below 0.77 (=23% attenuation) were not observed. Enhancement of UV radiation above the clear-sky value is relatively rare and does not exceed 8%.

[59] A similar transmittance analysis was also performed for the 400–600 nm integral. The associated distributions are presented in section S6.1 of the supplement (Figure S8). These distributions are qualitatively similar to the distributions for the 342.5–347.5 nm integral, but demonstrate that the effect of clouds is larger in the visible than the UV: average transmittance values vary between 0.876 and 0.971, and transmittance as low as 0.4 was observed on rare occasions.

6.1.1. Wavelength Dependence of Cloud Attenuation

[60] To investigate the wavelength dependence of cloud attenuation more systematically, we compared measured and modeled spectra for cloud and clear-sky conditions. Model clouds of varying optical depth were parameterized according to *Fu* [1996], assuming a homogeneous ice cloud layer (cirrostratus) between 5 and 6 km above sea level (2165–3165 m above ground) with an effective particle radius of 20 μm . These settings are in approximate agreement with measurements performed by *Mahesh et al.* [2001] at SPO. Figure 7 shows the ratios of cloud and clear-sky model spectra for SZAs between 0° and 85° , albedos of $\gamma = 0.05$ and 0.98, and cloud optical depths (COD) of $\tau = 0.5$ and 3.0. For SZAs between 70° and 85° , ratios of measured cloud and clear-sky spectra are also shown, which were selected from the Version 2 data set. Radiation levels varied by less than $\pm 0.5\%$ during these scans according to ancillary data from a UVA sensor, which is integral to the SUV-100 and samples continuously.

[61] Figure 7 supports the following conclusions: (1) The wavelength dependence of cloud attenuation derived from Version 2 spectra agrees with the model results to within $\pm 4\%$. This good agreement suggests that the model can help

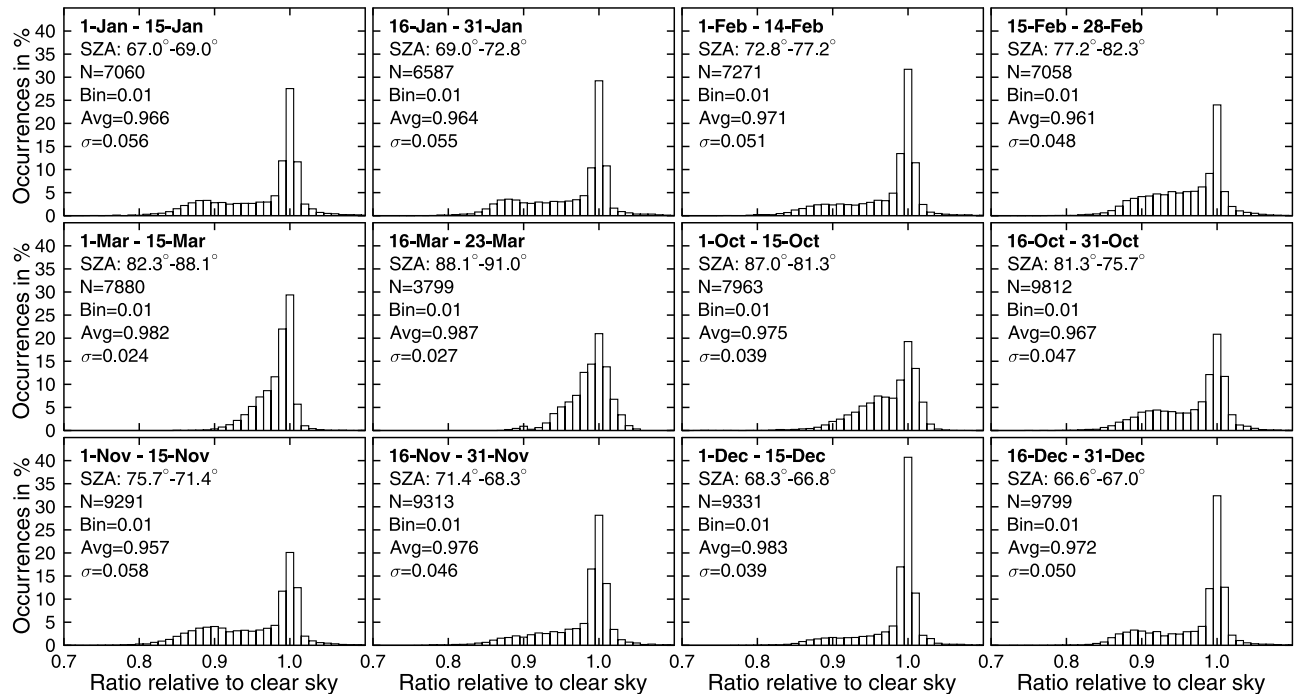


Figure 6. Frequency distributions $T(t)$ describing the ratio of spectral irradiance integrated over 342.5–347.5 nm to the associated clear sky irradiance. Each of the twelve plots refers to a different two-week period as indicated in the top left corner of each plot. SZA range, number of data points N , width of the histogram columns (Bin), average (Avg), and standard deviation (σ) of the distributions are also indicated. Only data from 1994–2003 have been used.

interpreting the measured effect. (2) Cloud attenuation is moderated by albedo. This is consistent with the observations by *Nichol et al.* [2003]. (3) The spectral effect of clouds increases with SZA. (4) For SZA larger than 60° , the wavelength dependence of cloud attenuation has similar characteristics for the high and low albedo case, but is less pronounced for high albedo. We quantify the wavelength dependence with the quotient $\zeta(\lambda_S, \lambda_L) = \rho(\lambda_S)/\rho(\lambda_L)$, where $\rho(\lambda_S)$ is the ratio of cloud and clear-sky spectra at λ_S , and

$\rho(\lambda_L)$ is the respective ratio at λ_L . For example at $\text{SZA} = 85^\circ$ and $\tau = 3.0$, $\zeta(330 \text{ nm}, 600 \text{ nm})$ is 1.81 for $\gamma = 0.05$ and 1.57 for $\gamma = 0.98$. (5) For low albedo, global irradiance under clouds is always smaller than for clear skies. (6) For low albedo and SZAs smaller than 50° , cloud attenuation is almost independent of SZA. (7) For high albedo and SZAs smaller than 50° , global irradiance under homogeneous clouds can be up to 20% higher than for clear skies. This result is interpreted below.

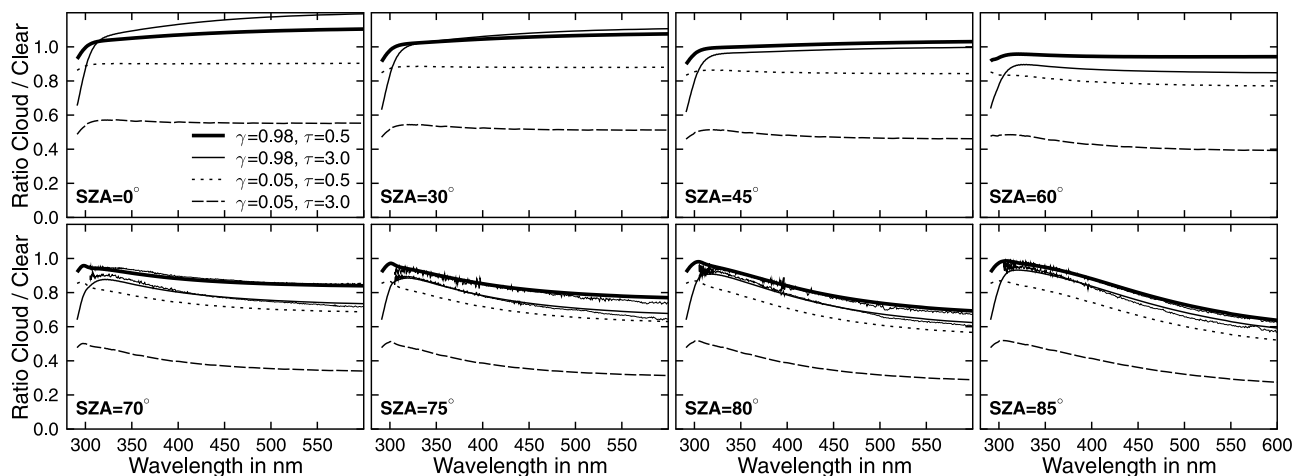


Figure 7. Ratio of cloud and clear-sky model spectra for SZAs between 0° (top left) and 85° (bottom right), surface albedos of $\gamma = 0.05$ and $\gamma = 0.98$, and cloud optical depths of $\tau = 0.5$ and $\tau = 3.0$. The bottom plots also include ratios of measured cloud and clear-sky spectra, which were selected from the Version 2 data set and indicated with thin, jagged lines.

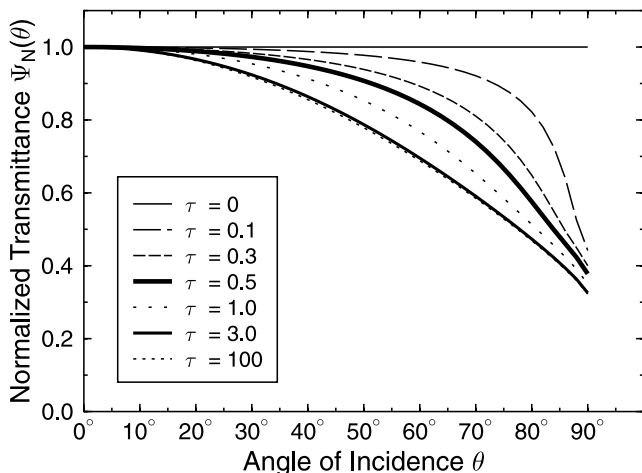


Figure 8. Normalized transmittance of ice cloud.

[62] Previous studies on the wavelength dependence of cloud extinction mainly focused on high-Sun situations. For example, *Seckmeyer et al.* [1996] studied cloud effects at $\text{SZA} = 59^\circ$, and found for their particular situation a cloud transmittance of 0.52 at 330 nm and 0.45 at 410 nm, resulting in $\zeta(330, 410) = 1.15$. This observation agrees well with our model calculations for $\text{SZA} = 60^\circ$, $\gamma = 0.05$, and $\tau = 3.0$, resulting in $\zeta(330, 410) = 1.13$. The wavelength effect of clouds at SPO is larger than at places studied previously due to large SZAs prevailing at SPO. Measurements near Boulder (section 5.2) indicate that wavelength dependence of cloud attenuation at large SZAs is consistent with the model calculations for $\gamma = 0.05$.

6.1.2. Physical Interpretation

[63] Our radiative transfer calculations indicate that the transmittance of a homogeneous cloud depends on the incidence angle θ of photons impinging on top of the cloud. This dependence can explain most of the predicted enhancement of surface irradiance at small SZAs and high albedo, as well as the strong wavelength dependence of cloud attenuation at large SZAs.

[64] For the following interpretation, we define cloud transmittance $\Psi(\theta)$ as irradiance below the cloud divided by irradiance above the cloud. We further define normalized cloud transmittance $\Psi_N(\theta)$ as the ratio of transmittance at incidence angle θ to transmittance at $\theta = 0^\circ$: $\Psi_N(\theta) = \Psi(\theta)/\Psi(0^\circ)$. Figure 8 shows $\Psi_N(\theta)$ at 450 nm as a function of θ for various cloud optical depths. The same cloud parameters as specified above were used for the calculation. Rayleigh scattering, molecular and particulate absorption, and ground reflection were switched off in the model. Thus Figure 8 shows the effect of the cloud on the radiative transfer with all other atmospheric processes excluded. $\Psi_N(\theta)$ decreases with increasing θ and increasing COD up to about $\tau = 3$, and remains constant for $\tau > 3$. The dependence of $\Psi_N(\theta)$ on θ can be explained by dominance of forward scattering in accordance with Mie theory. Similar calculations at 300 nm and 600 nm gave virtually identical results, confirming that scattering by an ensemble of ice particles is wavelength independent.

[65] We suggest the following explanation for the predicted enhancement of surface radiation by clouds at $\text{SZA} =$

0° and $\gamma = 1.00$: photons from the overhead Sun strike the cloud perpendicularly and pass through the cloud with a probably of $\Psi(0^\circ)$. If we ignore Rayleigh scattering between cloud and surface for sake of simplicity, all photons that passed through the cloud will be scattered upward by the snow covered ground. With the simplification that snow is a Lambertian reflector, scattered photons are isotropically distributed. Most upwelling photons will therefore strike the cloud at an incidence angle larger than zero and will have a probably of less than $\Psi(0^\circ)$ to escape through the cloud. The escape probability for an isotropic radiation field is $\Psi_I\Psi(0^\circ)$, where $\Psi_I = \int_{(2\pi)} \Psi_N(\theta) \cos(\theta) d\Omega / \int_{(2\pi)} \cos(\theta) d\Omega$ and Ω is solid angle. Calculation for $\tau = 3$ results in $\Psi_I = 0.80$. Multiple reflection between ground and cloud will incrementally increase surface irradiance. This can be described mathematically with a geometric series, resulting in a irradiance at the surface that is $1/\Psi_I = 1.25$ times the irradiance above the cloud. In the real atmosphere, Rayleigh scattering above the cloud ensures that not all photons from the overhead Sun strike the cloud perpendicularly. This leads to a reduction of cloud enhancement. Furthermore, cloud enhancement is smaller at shorter wavelengths because of the wavelength dependence of Rayleigh scattering. These effects quantitatively explain the wavelength dependence of enhancement indicated in the $\text{SZA} = 0^\circ$ panel of Figure 7.

[66] In the case of the large SZAs prevailing at SPO, radiation at short wavelengths above the cloud is mostly diffuse whereas irradiance at 600 nm has a large direct component for SZAs as high 85° . The simplest approach to calculate “effective cloud transmittance” $\Psi_{eff}(\theta, \lambda)$ for this case is to split the irradiance at the top of the cloud into a direct portion, $R(\theta, \lambda)$, and a diffuse portion, $1 - R(\theta, \lambda)$, and to assume that the diffuse portion is isotropic:

$$\Psi_{eff}(\theta, \lambda) = [R(\theta, \lambda)\Psi_N(\theta) + (1 - R(\theta, \lambda))\Psi_I]\Psi(0^\circ). \quad (5)$$

We calculated $R(85^\circ, \lambda)$ at the top of the cloud ($\tau = 3$) with the model to 15% at 330 nm and 87% at 600 nm. With these values, the effective transmittances at 330 nm and 600 nm are 0.741 $\Psi(0^\circ)$ and 0.457 $\Psi(0^\circ)$, respectively, and their ratio is 1.619. This value agrees within 2% with the $\zeta(330, 600)$ value derived from measurements. Table 2 compares measured and modeled $\zeta(330, 600)$ values with the ratios $\Psi_{eff}(\theta, 330 \text{ nm})/\Psi_{eff}(\theta, 600 \text{ nm})$ for SZAs between 70° and 85° . Effective transmittances agree reasonably well with the modeled $\zeta(330, 600)$ values, indicating that most (but not all) of the spectral dependence of cloud attenuation can be explained with the wavelength-dependent radiance distribution on top of the cloud and the incidence-angle-dependent cloud transmittance. One would expect that the wavelength dependence disappears at twilight when downwelling radiation is diffuse at all

Table 2. Spectral Cloud Effect Between 330 and 600 nm for $\tau = 3.0$

Cloud Effect	SZA			
	70°	75°	80°	85°
Measured $\zeta(330, 600)$	1.25	1.37	1.52	1.65
Modeled $\zeta(330, 600)$	1.19	1.30	1.44	1.57
$\Psi_{eff}(\theta, 330 \text{ nm})/\Psi_{eff}(\theta, 600 \text{ nm})$	1.13	1.21	1.36	1.62

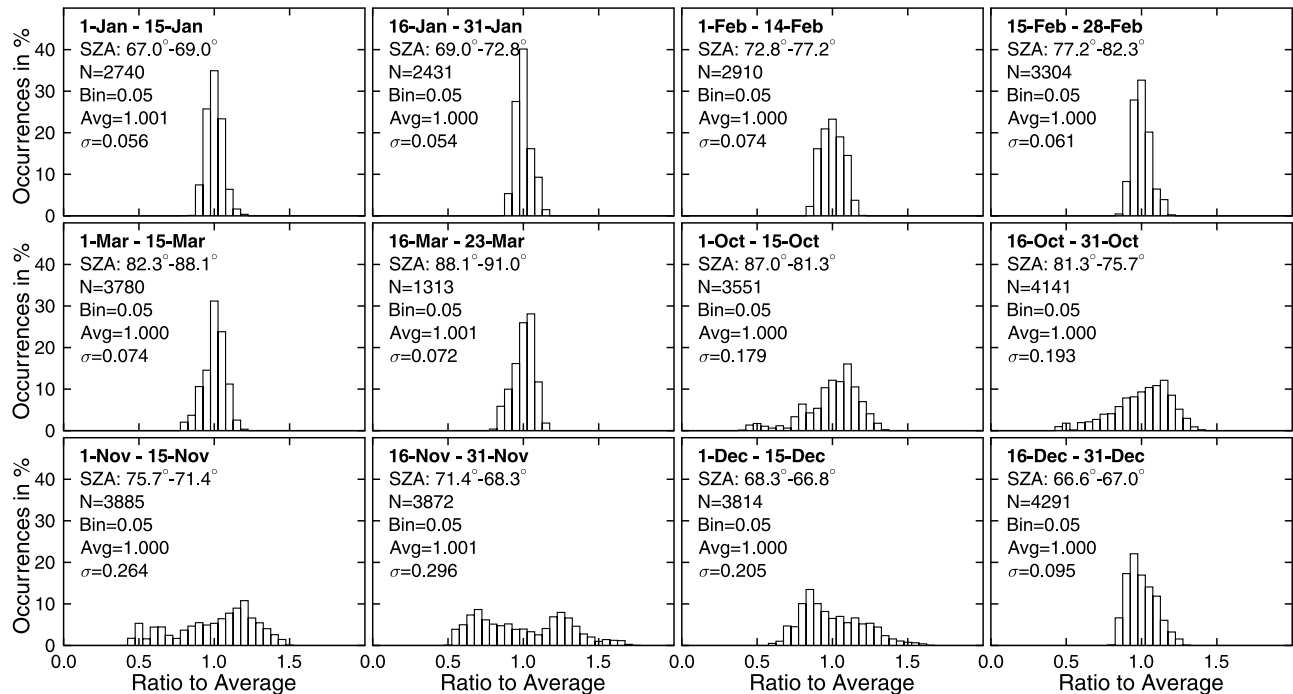


Figure 9. Frequency distribution of $V_{UVI}(t)$ describing the variation of UV index with respect to the average UV index of the years 1991–2003. Each of the twelve plots refers to a different two-week period as indicated in the top left corner of each plot. SZA range, number of data points N , width of the histogram columns (Bin), average (Avg), and standard deviation (σ) are indicated for every distribution. Data from 1991–2003 have been used.

wavelengths. Analysis of Version 2 spectra measured at SZAs $> 91^\circ$ indicates that this is indeed the case.

6.2. Variability in UV Due to Variations in Total Ozone

[67] The influence of total ozone on UV depends strongly on wavelength and therefore has to be evaluated separately for each wavelength or UV data product of interest. Here we focus on the UV index, denoted $E_{M,UVI}(t)$, and spectral irradiance at 305 nm, $E_{M,305}(t)$. To reduce the effect of clouds, we divided both quantities by $E_{M,345}(t)$:

$$\tilde{E}_{M,UVI}(t) = E_{M,UVI}(t)/E_{M,345}(t) \quad (6)$$

$$\tilde{E}_{M,305}(t) = E_{M,305}(t)/E_{M,345}(t).$$

This approach has been used by several authors [Lubin and Frederick, 1991; Diaz et al., 1996; Frederick et al., 1993] and is reasonable as the wavelength dependence of cloud attenuation between 305 and 345 nm is typically much smaller than the wavelength dependence introduced by variation in ozone. Model calculations indicate that differences in cloud attenuation between 305 and 345 nm are less than 5% for cloud optical depths below 1.0. Conditions with clear sky or clouds with optical depth less than 1.0 make up 85% of all cases at the South Pole (section 7). Normalization with $E_{M,345}(t)$ has the additional benefit of reducing remaining calibration differences between years.

[68] To quantify the year-to-year variability of $\tilde{E}_{M,UVI}(t)$, we selected data from different years that were measured at the same day and hour, and calculated their average. The

ratio of individual measurements to this average is then used to describe interannual variability. The ratio is denoted $V_{UVI}(t)$, and formally defined as:

$$V_{UVI}(t) = \frac{\tilde{E}_{M,UVI}(t)}{\frac{1}{n} \sum_{y \in [1991, 2003]} \tilde{E}_{M,UVI}(t - y(t) + \tilde{y})}. \quad (7)$$

The variable t is time in years, $y(t)$ is the integer part of t . $V_{UVI}(t)$ values are used for further analysis only, if at least data from 8 years contribute to the average.

[69] By comparing data measured at the same time but in different years, most of the dependence of UV index on SZA is removed. However, some SZA-dependence remains as the SZA at a given day and hour varies by a small amount from year to year. The variation is partly due to the fact that an astronomical year of approximately 365.25 days is forced into either 365 or 366 days. The variation is largest at equinox when it is $\pm 0.11^\circ$ ($\pm 1\sigma$). It is $\pm 0.09^\circ$ on 1 November, and disappears at solstice. We did not correct for the effect.

[70] Similar to the approach described in section 6.1., we constructed frequency distributions for $V_{UVI}(t)$ using data from all years and 0.05-wide bins. The distributions are presented in Figure 9 for the same twelve two-week periods used in Figure 6. Note that data from the first and last day of each period contribute with the same weight to the distribution, regardless of their SZA.

[71] Figure 9 illustrates that distributions for January–March are much narrower than distributions for October–December. During the first half of the year, less than 8% of

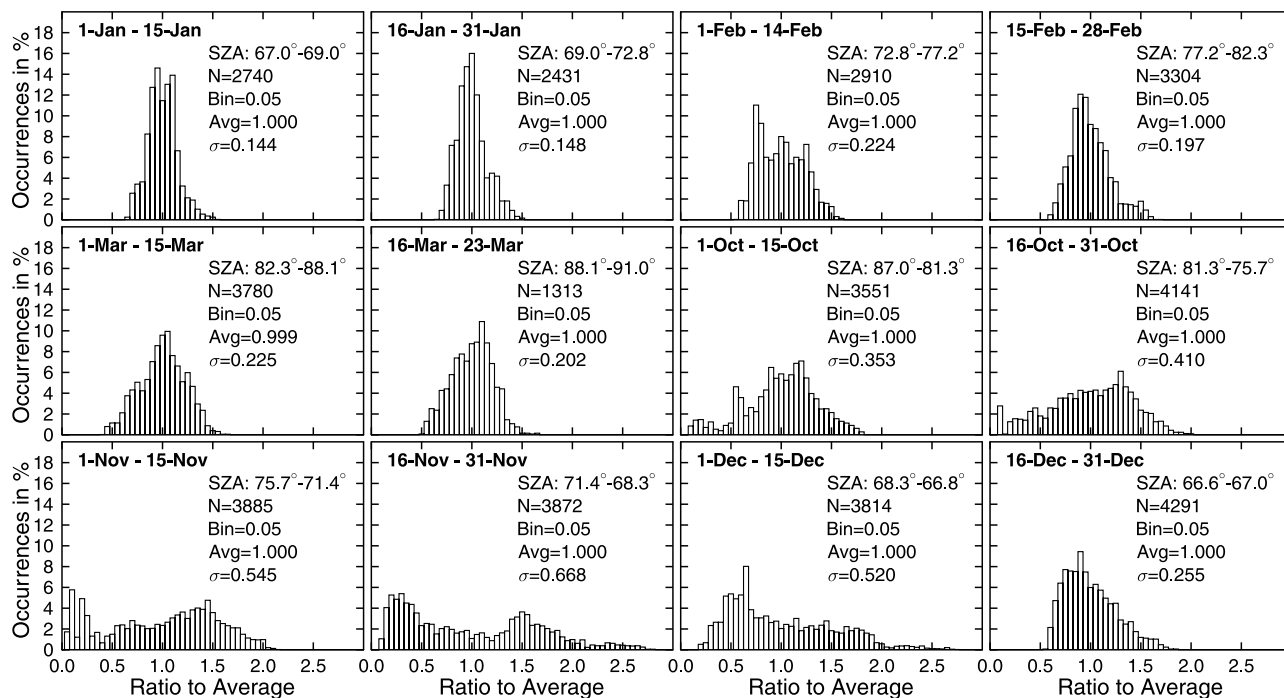


Figure 10. Frequency distribution of $V_{305}(t)$ describing the variation of spectral irradiance at 305 nm with respect to the average irradiance of the years 1991–2003. Each of the twelve plots refers to a different two-week period as indicated in the top left corner of each plot. SZA range, number of data points N , width of the histogram columns (Bin), average (Avg), and standard deviation (σ) are indicated for every distribution. Data from 1991–2003 have been used.

all $V_{UVI}(t)$ values differ by more than $\pm 12.5\%$ from unity. Standard deviations of the distributions are less than 0.074. For the period 1 October to 15 December, $V_{UVI}(t)$ values differ by up to 70% from unity, and the standard deviations of the distributions are on average 3.5 times as large as during the first half of the year. The broader distributions are mainly caused by the influence of the ozone hole, which typically disappears in late November and beginning of December [WMO, 2003]. Owing to the large variability in the “date of disappearance,” $V_{UVI}(t)$ distributions for the periods 15 November to 15 December are particularly wide.

[72] A comparison of Figures 6 and 9 suggests that during the first half of the year, the variability in UV introduced by clouds is comparable to the variability introduced by ozone. During the second part of the year, ozone is the dominating factor.

[73] $\tilde{E}_{M,305}(t)$ was processed in the same way as $\tilde{E}_{M,UVI}(t)$; the variability parameter associated with $\tilde{E}_{M,305}(t)$ is denoted $V_{305}(t)$. Frequency distributions for $V_{305}(t)$ are shown in Figure 10. Spectral irradiance at 305 nm is more strongly affected by ozone variations than the UV index. Distributions for $V_{305}(t)$ are therefore much broader than for $V_{UVI}(t)$; standard deviations for the same months are between a factor of 2 and 3.2 larger for the $V_{305}(t)$ distributions. During the first half of the year, $V_{305}(t)$ varies between 0.5 and 1.5. During the period affected by the ozone hole, $V_{305}(t)$ can be as low as 0.1 and as high as 2.7, implying that spectral irradiance at 305 nm may occasionally vary by up to a factor of 27 between two years. Distributions for November are bimodal. Lower and higher peaks relate to years with early

and late breakup of the ozone hole, respectively. The variability introduced by ozone exceeds that of cloud effects for all months.

6.3. Long-Term Changes in UV

[74] All analyses of the previous sections were based on instantaneous measurements. The analysis in this section is based on daily doses, calculated by integrating instantaneous measurements over 24 hour periods. Gaps in time series shorter than 7500 seconds were filled by spline interpolation. Days with gaps longer than 7500 seconds were excluded from further analysis. Finally, monthly averages of the daily doses were calculated. Only months with less than 6 missing days of data were used.

[75] Figure 11 shows monthly average daily doses of erythemal irradiance, DNA-damaging irradiance and the 342.5–347.5 nm integral for the months October–December. For erythemal and DNA-damaging daily doses, data show a large variation between different years due to the difference in total ozone. For example, the highest and lowest monthly average DNA-damaging daily doses differ by a factor of 5.8. In contrast, the variability for the 342.5–347.5 nm integral, which is not affected by ozone absorption, is low, indicating similar cloud cover in all years.

[76] Trend lines were calculated for all data sets by linear regression and are also shown in Figure 11. Slopes of the trend lines (expressed in change per decade relative to the year 1990), their 2-sigma uncertainty, and regression coefficients R^2 are given in the figure’s legend. Trends vary between -10% and $+8\%$ per decade but are not significant for any month. Values of R^2 are smaller or equal to 0.02,

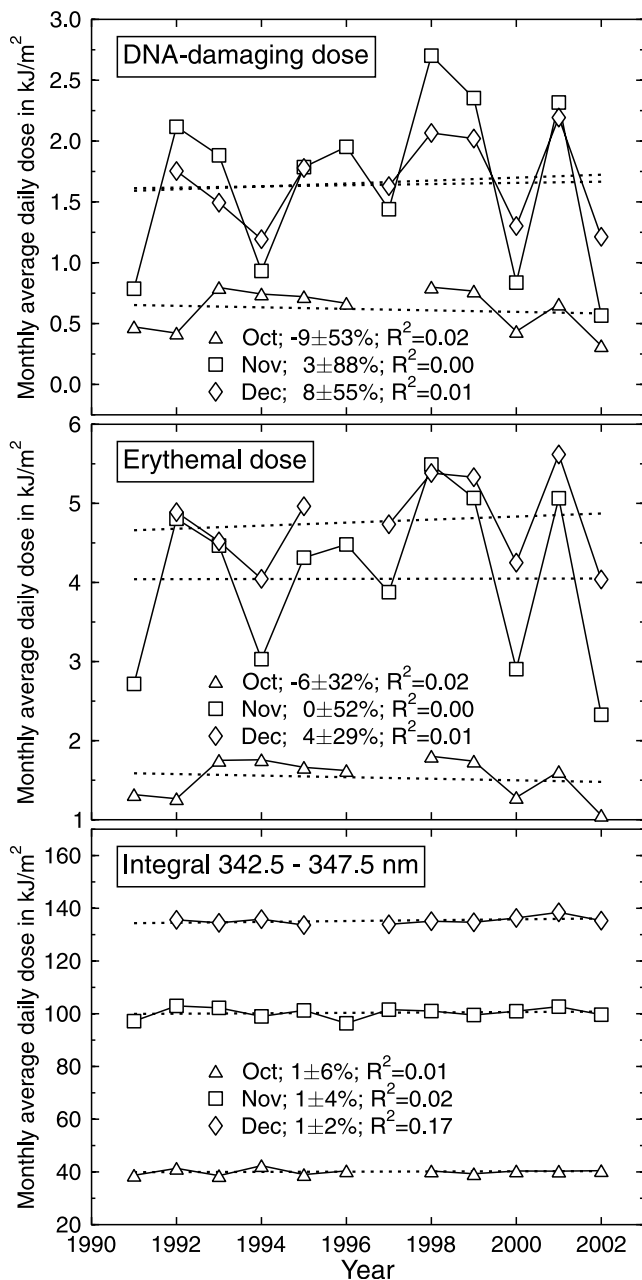


Figure 11. Time series of average monthly daily dose for months of October, November and December for three data products, namely (top) DNA-damaging dose, (center) erythema dose, and (bottom) the 342.5–347.5 nm integral. Dashed lines are trend lines determined by linear regression. Trend per decade, uncertainty of trend, and regression coefficient R^2 are indicated in the legend of each data product.

except on one occasion. The large interannual variability for erythema and DNA-damaging doses clearly obscures any linear trend, if it exists. For November, omission of one year of data at the beginning or end of the time series would change the sign of the trend lines. December doses of the 342.5–347.5 nm integral are on average 33% higher than November doses due to the smaller SZA in December. In contrast, trend lines for DNA-damaging irradiance for both

months are nearly identical, indicating that the effect of the smaller SZA in December is offset by the lower total ozone values in November.

7. Discussion and Conclusions

[77] UV measurements of the NSF/OPP UV Monitoring Network have been corrected for wavelength and cosine errors, and have been normalized to a uniform band pass of 1.0 nm FWHM. The resulting new data set “Version 2” will supersede the originally published Version 0 data. Version 2 data have higher accuracy and feature a larger number of data products (section S7). A comprehensive uncertainty budget was also established, and the data set was compared to results of a radiative transfer model as well as measurements at low latitude sites to further assess its quality and homogeneity. Lastly, a climatology of UV radiation at the South Pole was established, focusing on the influence of clouds, ozone variability, the effect of aerosols from volcanic eruptions, and changes of UV radiation over time.

[78] Some parameters for the correction procedures were based on assumptions due to the lack of appropriate characterization data. For example, the cosine error of the SUV-100 spectroradiometer for zenith angles larger than 70° was estimated by comparing measurement and model at 600 nm (section S2.3). This procedure is not ideal but is the only feasible approach in absence of annual laboratory characterizations of the instrument’s angular response. Clearly, if model calculations were wrong, the estimated angular response would be incorrect as well. On the basis of the following evidence we believe that this is not the case:

[79] 1. At $SZA = 70^\circ$, model-based estimates of the angular response agreed with the measurements of a test apparatus to within $\pm 2\%$ (Figures S2 and S4).

[80] 2. Ratios of Version 2 spectra to model spectra from the South Pole display a very similar pattern as ratios of SUV-150B spectra to associated model spectra evaluated for measurements performed at Boulder and San Diego (Figure 2A). If the cosine correction of SPO data were incorrect, both ratios would display a different pattern as the effect of the cosine error increases with wavelength. The good agreement of the three data sets is achieved despite the vastly different atmospheric conditions at the South Pole and the other two sites, and the angular response differences of the SUV-100 and SUV-150B.

[81] 3. Version 2 measurements of different years are very consistent (Figure 3) despite the change of angular response introduced by the collector change in January 2000.

[82] 4. Version 2 spectral irradiance data were compared with measurements of a GUV-541 multifilter radiometer from BSI, which was installed at SPO in January 2003. At 380 nm (largest wavelength of the GUV-541), the ratio of the two data sets varied by less than $\pm 4\%$ as a function of SZA for SZAs between 67° and 92° . A more detailed analysis is limited by uncertainties in the GUV-541 cosine correction and possible drifts of the two instruments against each other.

[83] Despite these indicators, we cannot rule out errors in the estimate of the cosine error f_B at zenith angles (ZA) larger than 80° . The uncertainty of f_B is therefore considerable, and reaches $\pm 4\%$ ($\pm 1\sigma$) at $ZA = 80^\circ$; and $\pm 7\%$ at $ZA = 85^\circ$. Some of the uncertainty of f_B is caused by the large

effect of even small amounts of aerosols on the ratio of direct-to-global irradiance. This uncertainty is further discussed in section S7 of the supplement. Even though systematic errors cannot be excluded, Figure 3 demonstrates that the Version 2 data set is in itself consistent and homogeneous. This is particularly important for investigations into changes in UV over longer timescales, and becomes essential in the future when additional years of measurement make reliable trend determinations feasible.

[84] The uncertainty of Version 2 data is largest during periods with variable, thin clouds, which lead to little attenuation but a spatial redistribution of radiation. For some spectra measured during these periods, a clear-sky cosine corrections may have been applied while scaling of the measured irradiance with the constant correction factor for overcast skies would have been more appropriate, or vice versa. Situations with CODs less than 0.3 are particularly affected. These situations are quite frequent at SPO: from the 119068 spectra that are part of Version 2, 51% are clear sky or have a COD of smaller than 0.05, 23% have a COD between 0.05 and 0.3, and 26% have a COD of larger than 0.3. Roughly one quarter of the data set therefore falls within the highest uncertainty category of Table 1.

[85] Version 2 and Version 0 data differ by more than 30% in extreme cases, e.g., when wavelength is larger than 500 nm and SZA larger than 80° (Figure S7). Differences for biologically relevant dose rates, as well as UV-B and UV-A irradiance, are typically smaller than 12% and vary by less than 5% within a given volume. These differences are considerably smaller than changes introduced by the variability of atmospheric ozone concentration (Figures 9 and 10). Hence conclusions drawn from previously published studies (which were all based on Version 0 UV data) are still valid. This is particularly the case for investigations on relative changes of UV. When absolute data accuracy was critical (e.g., when comparing network data with satellite observations [Kalliskota et al., 2000]), authors considered in their conclusions that Version 0 data are not cosine corrected.

[86] The expanded uncertainty of Version 2 UV data ranges between 4.6% and 7.2% (Table 1). These uncertainties may appear large, but are comparable to uncertainties of similar instruments [Bais et al., 1997; Bernhard and Seckmeyer, 1999; Hofzumahaus et al., 1999]. Uncertainties for some volumes may be higher or lower. We advise data users to consider the information given in sections S3.1–S3.8 of the supplement, and to consult Network Operations Reports before using data of a particular volume.

[87] Measurements during cloudless periods in the austral spring of 1991 were substantially lower than measurements of other years (Figure 3). Model calculations indicate that this anomaly can be explained with effects of aerosols from the eruption of Cerro Hudson, which took place in August 1991. According to measurements performed by CMDL [2002] between October 1991 and January 1992, monthly average aerosol optical depth anomalies in the 530–690 nm range varied between 0.21 and 0.275. Ratios of model spectra calculated with and without aerosols (Figure 4) agreed quantitatively with the anomaly seen in the measurements (Figure 3). The strong wavelength dependence of aerosol attenuation that is apparent in Figure 4 is possibly caused by the same mechanism that is responsible for the

wavelength dependence of cloud attenuation (section 6.1.2). Model calculations by Michelangeli et al. [1992] and Davies [1993], suggest that a volcanic aerosol layer may lead to large relative increases in surface UV irradiance at wavelengths below approximately 295 nm, in particular at large SZAs and for high surface albedo. Such increases are not evident in our data since spectral irradiance at 295 nm or shorter wavelengths is below the detection limit of SUV-100 measurements.

[88] The average attenuation of UV irradiance at 345 nm by clouds is less than 5% and no attenuations greater than 23% were observed (Figure 6). The reduction of UV radiation by clouds at SPO is much smaller than at the Antarctic peninsula, where daily mean attenuations range between 20% and 60%, and maximum reductions exceed 80% [Lubin et al., 1992]. At 60° South, zonally averaged minimum daily UV-B cloud transmission ranges between approximately 0.45 and 0.65, depending on season [Lubin et al., 1998]. The comparatively little influence of clouds at SPO is due to high surface albedo, which diminishes cloud attenuation [Nichol et al., 2003], and the low atmospheric water content, which leads to optically thin clouds with little vertical development. According to our calculations, 71% of all clouds at SPO have an optical depth between 0 and 1. The fraction of clouds with CODs between 1 and 5 and CODs larger than 5 is 16% and 13%, respectively. This result is in good agreement with observations at SPO by Mahesh et al. [2001], who determined frequencies of 65%, 24% and 11% for the three COD ranges using longwave emission spectroscopy. In contrast, COD values at 630 nm at the Antarctic peninsula range between 20 and 50, with a most probable value of 25 [Ricchiuzzi et al., 1995].

[89] Our data indicate that attenuation by clouds at the SPO increases with wavelength (section 6.1.1). This wavelength dependence tends to be larger than at places studied previously. For example, Seckmeyer et al. [1996] examined cloud effects at SZA = 59° and found a difference in transmittance of 15% between 330 nm and 410 nm. Differences between the same two wavelengths at SPO can be as high as 19%. A physical interpretation of the wavelength dependence reported by Seckmeyer et al. [1996] was provided by Kylling et al. [1997]. In their explanation, photons that are reflected upward by the cloud and then scattered downward by Rayleigh scattering at air molecules above the cloud lead to enhanced irradiance at the surface. The wavelength effect is explained with the wavelength dependence of Rayleigh scattering. The same mechanism is not applicable for SPO: clouds at SPO do not create an additional upward flux since photons are already reflected upward by the snow covered surface. Model calculations presented in section 6.1.2 suggest that the wavelength dependence of cloud attenuation at SPO is instead caused by the wavelength-dependent radiance distribution on top of the cloud and the dependence of cloud transmittance on the angle of incidence. These model calculations also predict that homogeneous ice clouds can increase global irradiance by up to 20% above the clear-sky level, if the Sun is overhead and surface albedo is very high. This prediction has yet to be confirmed with measurements. A verification is challenging since a place with very high and homogeneous albedo, overhead Sun, and optically thin clouds may not exist.

[90] Time series of DNA-damaging irradiance and of the UV index demonstrated the large impact of variations of total ozone column on UV (Figure 9). Largest radiation levels typically occur in late November and early December when low ozone columns coincide with relatively small SZAs. The highest DNA-damaging irradiance was measured on 11/30/98 and was $5.6 \mu\text{W}/\text{cm}^2$. When the ozone hole breaks down, DNA-damaging irradiance can decrease by more than a factor of two within two days. Typical summer UV index values range between 2.0 and 3.5, with a maximum value of 4.0 measured on 11/30/98. These values are clearly smaller than typical summer values for midlatitudes. However, South Pole has 24 hours of sunlight, which partly compensates the latitude effect when daily doses are considered. Average daily erythemal doses for the SPO and San Diego are equal during summer, and maximum erythemal daily doses at SPO exceed those of San Diego [Bernhard et al., 2003a].

[91] The year-to-year variation of UV is much higher in the austral spring than in the fall due to the influence of the ozone hole (Figures 9 and 10). In November and December, the UV index can in some years differ by more than a factor of 1.5 from the average. On average, the UV index in the last two weeks in November varies by $\pm 30\%$ ($\pm 1\sigma$) between different years. During the first half of the year, the variability in the UV index introduced by ozone is comparable to the variability introduced by clouds. During the second part of the year, ozone is the dominating factor.

[92] The variability of UV is generally higher at shorter wavelengths. For spectral irradiance at 305 nm (Figure 10), the year-to-year variation is on average 55–67% for the period 1 November to 15 December. In extreme cases, spectral irradiance at a given day can differ by up to a factor of 27 between two years. For all months, the variability introduced by ozone exceeds that of cloud effects.

[93] Linear regression analyses of time series of monthly average daily doses of erythemal irradiance, DNA-damaging irradiance, and the 342.5–347.5 nm integral did not indicate statistically significant trends in UV (Figure 11). It is unlikely that more sophisticated statistical analysis (for example by removing variability from natural cycles, such as the 11-year solar cycle and the QBO, and by considering autocorrelation in the data sets) would lead to different conclusions. Weatherhead et al. [1998] have shown that it may require 45 ± 10 years to detect a linear trend in total ozone of 5%/decade at the South Pole at the 2σ confidence level. Although newer results suggest that the time required for trend detection may be smaller [Reinsel et al., 2002], it is still considerably longer than the Version 2 data set. On the basis of proxy data, Diaz et al. [2003] have shown that UV irradiance at the South Pole has significantly changed since the 1970s due to the appearance of the ozone hole in the 1980s. As the NSF/OPP UV monitoring network was established only after the ozone hole had been discovered, no data are available to directly compare current UV measurements with data from the preozone hole era. Measurements between the years 1991–2002 document variability on an elevated level.

[94] **Acknowledgments.** The NSF/OPP UV Monitoring Network is operated and maintained by Biospherical Instruments Inc. under a contract

from the NSF Office of Polar Programs via Raytheon Polar Services Company (RPSC). G. Harris from Research Instrument Systems designed and built the first prototype of the SUV-100. We wish to express our gratitude to numerous operators of the SUV-100 spectroradiometer at SPO. Further thanks go to R.D. McPeters from NASA for providing TOMS data, S. Oltmans from NOAA/CMDL for Dobson total ozone and ozone profile data, C. Gueymard from Solar Consulting Services for discussions related to extraterrestrial spectra, and B. Mayer from DLR, Germany, for calculations and discussions on cloud effects.

References

- Anderson, G. P., S. A. Clough, F. X. Kneizys, J. H. Chetwynd, and E. O. Shettle (1986), AFGL atmospheric constituents profiles (0–120 km), *Tech. Rep. AFGL-TR-86-0110*, Air Force Geophys. Lab., Bedford, Mass.
- Bais, A. F., M. Blumthaler, A. R. Webb, J. Gröbner, P. J. Kirsch, B. G. Gardiner, C. S. Zerefos, T. Svenoe, and T. J. Martin (1997), Spectral UV measurements over Europe within the Second European Stratospheric Arctic and Midlatitude Experiment activities, *J. Geophys. Res.*, **102**(D7), 8731–8736.
- Bass, A., and R. J. Paur (1985), The ultraviolet cross sections of ozone: I, The measurement, in *Atmospheric Ozone*, edited by C. Zerefos and A. Ghazi, pp. 606–616, D. Reidel, Norwell, Mass.
- Bernhard, G., and G. Seckmeyer (1999), Uncertainty of measurements of spectral solar UV irradiance, *J. Geophys. Res.*, **104**(D12), 14,321–14,345.
- Bernhard, G., C. R. Booth, and J. C. Ehemjian (2002), Comparison of measured and modeled spectral ultraviolet irradiance at Antarctic stations used to determine biases in total ozone data from various sources, in *Ultraviolet Ground- and Space-Based Measurements, Models, and Effects*, *SPIE Int. Soc. Opt. Eng.*, vol. 4482, edited by J. R. Slusser, J. R. Herman, and W. Gao, pp. 115–126, Int. Soc. Opt. Eng., Bellingham, Wash. (Available at www.biospherical.com/nsf/presentations.asp)
- Bernhard, G., C. R. Booth, J. C. Ehemjian, V. V. Quang, and S. A. Lynch (2003a), NSF Polar Programs UV Spectroradiometer Network 2000–2001 Operations Report, Biospherical Instrum., San Diego, Calif. (Available at www.biospherical.com/NSF)
- Bernhard, G., C. R. Booth, and R. D. McPeters (2003b), Calculation of total column ozone from global UV spectra at high latitudes, *J. Geophys. Res.*, **108**(D17), 4532, doi:10.1029/2003JD003450.
- Booth, C. R., and S. Madronich (1994), Radiation amplification factors: Improved formulation accounts for large increases, in *Ultraviolet Radiation in Antarctica, Measurements and Biological Effects*, *Antarc. Res. Ser.*, vol. 62, edited by C. S. Weiler and P. A. Penhale, pp. 39–42, AGU, Washington, D. C.
- Booth, C. R., T. B. Lucas, J. H. Morrow, C. S. Weiler, and P. A. Penhale (1994), The United States National Science Foundation's polar network for monitoring ultraviolet radiation, in *Ultraviolet Radiation in Antarctica: Measurements and Biological Effects*, *Antarc. Res. Ser.*, vol. 62, edited by C. S. Weiler and P. A. Penhale, pp. 17–37, AGU, Washington, D. C.
- Bush, B. C., F. P. J. Valero, A. S. Simpson, and L. Bignone (2000), Characterization of thermal effects in pyranometers: A data correction algorithm for improved measurement of surface insolation, *J. Atmos. Ocean. Technol.*, **17**, 165–175.
- Climate Monitoring and Diagnostics Laboratory (CMDL) (2002), Climate Monitoring and Diagnostics Laboratory Summary, *Rep. 26 2000–2001*, edited by D. B. King et al., U. S. Dept. of Comm., Boulder, Colo.
- Davies, R. (1993), Increased transmission of ultraviolet radiation to the surface due to stratospheric scattering, *J. Geophys. Res.*, **98**(D4), 7251–7253.
- Deshler, T., A. Adriani, G. P. Gobbi, D. J. Hofmann, G. Di Donfrancesco, and B. J. Johnson (1992), Volcanic aerosol and ozone depletion within the Antarctic polar vortex during the austral spring of 1991, *Geophys. Res. Lett.*, **19**(18), 1819–1822.
- Diaz, S. B., J. E. Frederick, T. Lucas, C. R. Booth, and I. Smolskaia (1996), Solar ultraviolet irradiance at Tierra del Fuego: Comparison of measurements and calculations over a full annual cycle, *Geophys. Res. Lett.*, **23**(4), 355–358.
- Diaz, S., D. Nelson, G. Deferrari, and C. Camili6n (2003), A model to extend spectral and multiwavelength UV irradiances time series: Model development and validation, *J. Geophys. Res.*, **108**(D4), 4150, doi:10.1029/2002JD002134.
- Dutton, E. G., and J. R. Christy (1992), Solar radiative forcing at selected locations and evidence for global lower tropospheric cooling following the eruptions of El Chichon and Pinatubo, *Geophys. Res. Lett.*, **19**(23), 2313–2316.
- Frederick, J. E., P. F. Soulen, S. B. Diaz, I. Smolskaia, C. R. Booth, T. B. Lucas, and D. A. Neuschuler (1993), Solar ultraviolet irradiance observed from southern Argentina: September 1990 to March 1991, *J. Geophys. Res.*, **98**(D5), 8891–8897.

- Fu, Q. (1996), An accurate parameterization of the solar radiative properties of cirrus clouds for climate models, *J. Climate*, 9, 2058–2082.
- Grenfell, T. C., S. G. Warren, and P. C. Mullen (1994), Reflection of solar radiation by the Antarctic snow surface at ultraviolet, visible, and near-infrared wavelengths, *J. Geophys. Res.*, 99(D9), 18,669–18,684.
- Gueymard, C. A. (2004), The sun's total and spectral irradiance for solar energy applications and solar radiation models, *Sol. Energy*, 76(4), 423–453.
- Harrison, L., P. Kiedron, and J. Schlemmer (2003), Extraterrestrial solar spectrum 360–1050 nm from rotating shadowband spectroradiometer measurements at the Southern Great Plains (ARM) site, *J. Geophys. Res.*, 108(D14), 4424, doi:10.1029/2001JD001311.
- Hofzumahaus, A., A. Kraus, and M. Müller (1999), Solar actinic flux spectroradiometry: A technique for measuring photolysis frequencies in the atmosphere, *Appl. Opt.*, 38(21), 4443–4460.
- Holben, B. N., et al. (1998), AERONET—A federated instrument network and data archive for aerosol characterization, *Remote Sens. Environ.*, 66, 1–16.
- Kalliskota, S., J. Kaurola, P. Taalas, J. Herman, E. Celarier, and N. Krotkov (2000), Comparison of daily UV doses estimated from Nimbus 7/TOMS measurements and ground-based spectroradiometric data, *J. Geophys. Res.*, 105(D4), 5059–5067.
- Kato, S., T. P. Ackerman, E. E. Clothiaux, J. H. Mather, G. G. Mace, M. L. Wesely, F. Murcray, and J. Michalsky (1997), Uncertainties in modeled and measured clear-sky surface shortwave irradiances, *J. Geophys. Res.*, 102(D22), 25,881–25,898.
- Kaye, J. A., and T. L. Miller (1996), The ATLAS series of shuttle missions, *Geophys. Res. Lett.*, 23(17), 2285–2288.
- Kurucz, R. L., I. Furenlid, J. Brault, and L. Testerman (1984), Solar flux atlas from 296 to 1300 nm, Natl. Sol. Observ. Atlas. 1, Harvard Univ. Press, Cambridge, Mass. (Available at ftp://ftp.noao.edu/fts/fluxat/)
- Kylling, A., A. Albold, and G. Seckmeyer (1997), Transmittance of a cloud is wavelength-dependent in the UV-range: Physical interpretation, *Geophys. Res. Lett.*, 24(4), 397–400.
- Lubin, D., and J. E. Frederick (1991), The ultraviolet radiation environment of the Antarctic Peninsula: The roles of ozone and cloud cover, *J. Appl. Meteorol.*, 30(4), 478–493.
- Lubin, D., B. G. Mitchell, J. E. Frederick, A. D. Alberts, C. R. Booth, T. B. Lucas, and D. A. Neuschuler (1992), A contribution toward understanding the biospherical significance of Antarctic ozone depletion, *J. Geophys. Res.*, 97(D8), 7817–7828.
- Lubin, D., E. H. Jensen, and H. P. Gies (1998), Global surface ultraviolet radiation climatology from TOMS and ERBE data, *J. Geophys. Res.*, 103(D20), 26,061–26,091.
- Madronich, S. (1993), UV radiation in the natural and perturbed atmosphere, in *Environmental Effects of UV (Ultraviolet) Radiation*, edited by M. Tevini, pp. 17–69, Lewis Publ., Boca Raton, Fla.
- Mahesh, A., V. P. Walden, and S. G. Warren (2001), Ground-based infrared remote sensing of cloud properties over the Antarctic plateau. Part II: Cloud optical depths and particle sizes, *J. Appl. Meteorol.*, 40, 1279–1294.
- Mayer, B., G. Seckmeyer, and A. Kylling (1997), Systematic long-term comparison of spectral UV measurements and UVSPEC modeling results, *J. Geophys. Res.*, 102(D7), 8755–8768.
- McKinlay, A. F., and B. L. Diffey (Eds.) (1987), A reference action spectrum for ultraviolet induced erythema in human skin, *CIE Res. Note*, 6(1), 17–22.
- Michalsky, J. J., P. Kiedron, Q. Min, and L. Harrison (2003), Shortwave clear-sky diffuse irradiance in the 300- to 1100-nm range: Comparison of models with UV-VIS-NIR RSS and broadband radiometer measurements at the Southern Great Plains ARM site in September/October 2001, in *Ultraviolet Ground- and Space-Based Measurements, Models, and Effects III, SPIE Int. Soc. Opt. Eng.*, vol. 5156, edited by J. R. Slusser, J. R. Herman, and W. Gao, pp. 74–84, Int. Soc. Opt. Eng., Bellingham, Wash.
- Michelangeli, D. V., M. Allen, Y. L. Young, R.-L. Shia, D. Crisp, and J. Eluszkiewicz (1992), Enhancement of atmospheric radiation by an atmospheric aerosol layer, *J. Geophys. Res.*, 97(D1), 865–874.
- Mlawer, E. J., P. D. Brown, S. A. Clough, L. C. Harrison, J. J. Michalsky, P. W. Kiedron, and T. Shippert (2000), Comparison of spectral direct and diffuse solar irradiance measurements and calculations for cloudfree conditions, *Geophys. Res. Lett.*, 27, 2653–2656.
- Naus, H., and W. Ubachs (1999), Visible absorption bands of the (O₂)₂ collision complex at pressures below 760 Torr, *Appl. Opt.*, 38(15), 3423–3428.
- Nichol, S. E., G. Pfister, G. E. Bodeker, R. L. McKenzie, S. W. Wood, and G. Bernhard (2003), Moderation of cloud reduction of UV in the Antarctic due to high surface albedo, *J. Appl. Meteorol.*, 42(8), 1174–1183.
- Reinsel, G. C., E. Weatherhead, G. C. Tiao, A. J. Miller, R. M. Nagatani, D. J. Wuebbles, and L. E. Flynn (2002), On detection of turnaround and recovery in trend for ozone, *J. Geophys. Res.*, 107(D10), 4078, doi:10.1029/2001JD000500.
- Ricchiuzzi, P., C. Gautier, and D. Lubin (1995), Cloud scattering optical depth and local surface albedo in the Antarctic: Simultaneous retrieval using ground-based radiometry, *J. Geophys. Res.*, 100(D10), 21,091–21,104.
- Schmid, B., and C. Wehrli (1995), Comparison of Sun photometer calibrations by use of the Langley technique and the standard lamp, *Appl. Opt.*, 34(21), 4500–4512.
- Seckmeyer, G., R. Erb, and A. Albold (1996), Transmission of a cloud is wavelength-dependent in the UV-range, *Geophys. Res. Lett.*, 23(20), 2753–2755.
- Setlow, R. B. (1974), The wavelength in sunlight effective in producing skin cancer: A theoretical analysis, *Proc. Natl. Acad. Sci. U.S.A.*, 71(9), 3363–3366.
- Shaw, G. E. (1982), Atmospheric turbidity in the polar regions, *J. Appl. Meteorol.*, 21, 1080–1088.
- United Nations Environment Programme (UNEP) (1991), *Environmental Effects Of Ozone Depletion: 1991 Update*, edited by J. C. van der Leun, M. Tevini, and R. C. Worrest, U. N. Environ Programme, Nairobi.
- vanHoosier, M. E. (1996), Solar ultraviolet spectral irradiance data with increased wavelength and irradiance accuracy, in *Ultraviolet Atmospheric and Space Remote Sensing: Methods and Instrumentation, Proc., SPIE Int. Soc. Opt. Eng.*, vol. 2831, edited by R. E. Huffman and C. G. Stergis, pp. 57–64, Int. Soc. Opt. Eng., Bellingham, Wash.
- Weatherhead, E. C., et al. (1998), Factors affecting the detection of trends: Statistical considerations and applications to environmental data, *J. Geophys. Res.*, 103(D14), 17,149–17,161.
- World Meteorology Organization (WMO) (1998), Report of the WMO-WHO meeting of experts on standardization of UV indices and their dissemination to the public, *Global Atmos. Watch Rep. 127*, Geneva.
- World Meteorology Organization (WMO) (2003), Scientific assessment of ozone depletion: 2002, Global ozone research and monitoring project, *Rep. 47*, 498 pp., Geneva.

G. Bernhard, C. R. Booth, and J. C. Eshramjian, Biospherical Instruments Inc., 5340 Riley Street, San Diego, CA 92110, USA. (bernhard@biospherical.com; booth@biospherical.com; jime@biospherical.com)

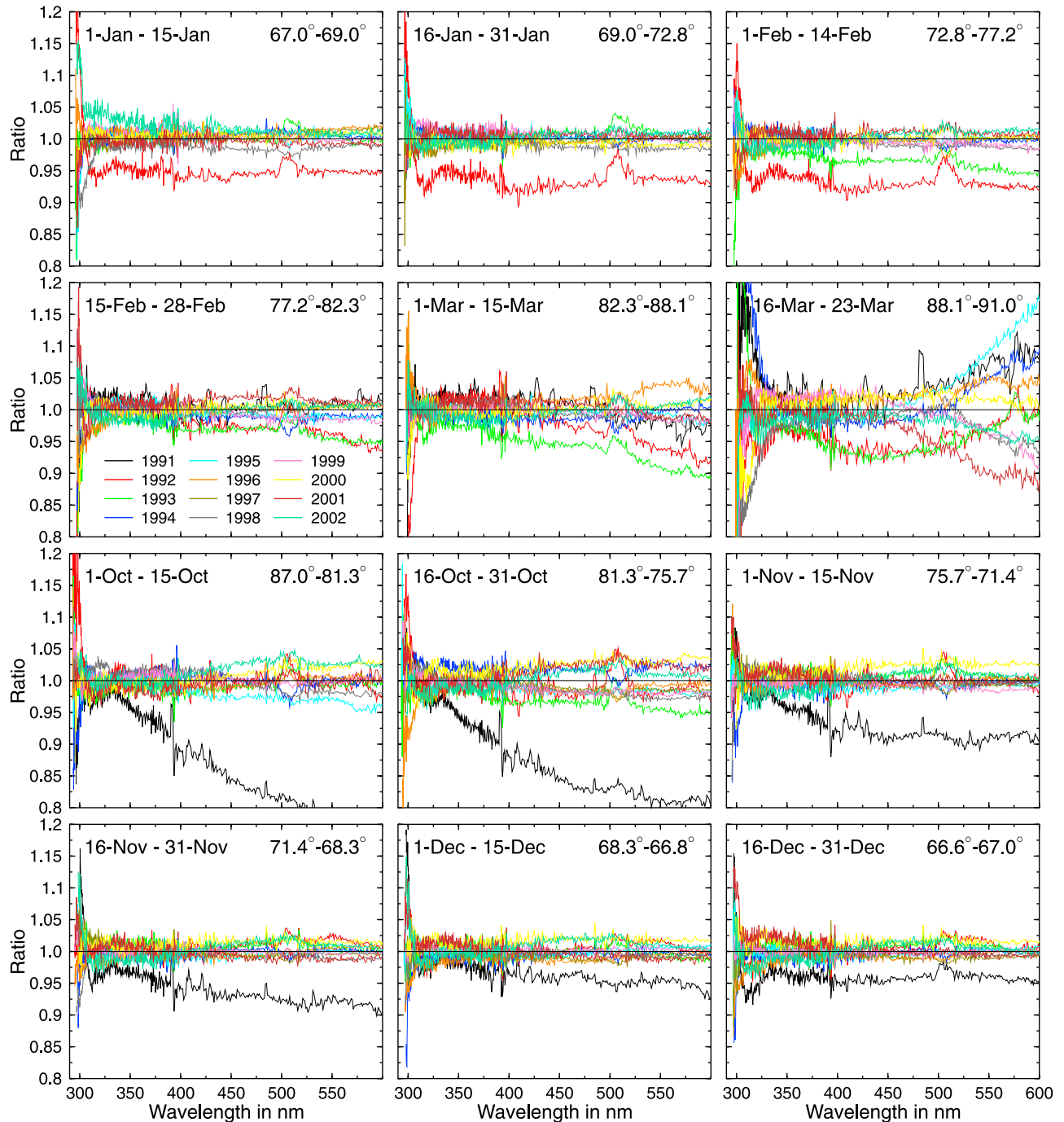


Figure 3. Normalized ratios $Q(\lambda, p, y)$ of measurement and model. Each plot shows $Q(\lambda, p, y)$ for a different two-week period, indicated in the top left corner of each plot. The SZA range for these periods is indicated in the top right corner. Data from each year are coded in a different grayscale level or color, assigned in the legend of the plot for the period 15–28 February.